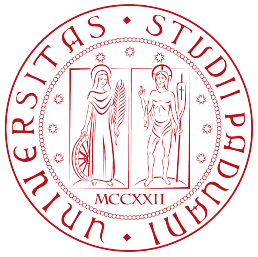

UNIVERSITÀ DEGLI STUDI DI PADOVA

Department of Physics and Astronomy "Galileo Galilei"

Astrophysics and Cosmology Master Degree

Tip-Tilt correction with

Fast Refractive Modulator in a telescope

Supervisor

Prof. Sergio Ortolani

Co-Supervisors

Dr. Stefano Bonora

Mr. Antonio Vanzo

Student

Kevin Campaci

mat.1238632

Academic year 2021/2022

Dedico questo lavoro al me stesso
del futuro, che rappresenti l'inizio
di una vita ricca di emozioni
e priva di rimpianti. Lo dedico
alla mia famiglia, alle persone che
mi vogliono bene e alla mia speciale
compagna di viaggio.

Grazie.

Kevin del 2022

Contents

Introduction

Nowadays, telecommunications are of fundamental importance in all areas, from work to simple leisure. However, there are still many areas that are not yet reached by good telecommunications and internet infrastructures. From an overview of 2020 by IDate[1] results that the 41% of houses in Italy are reached by FTTH (Fiber To The Home) technology, over 10% with respect to the precedent year but not yet encouraging because the optical fiber diffusion is behind the European average positioning Italy at the 18th place in UE and 27th among 39 Europeans countries. In particular the less supplied areas are surely those near the small centers where the number of residents touch the thousand of units; in these small realities the installation of underground fiber optics is complex due to high costs and the presence of natural obstacles such as rivers, lakes or other barriers that would impose a much higher architectural effort. Less than 70% of families in areas with less than 2000 inhabitants are reached by an internet connection (38). With the continued digitization of many services and activities these families find themselves in an uncomfortable situation instead of being helped by the advent of technology; so it would be useful to find an alternative solution to underground fiber optics that could give the same type of connection to families or workplaces that are not necessarily located in large city centers.
FSO communications are optical wireless communication which operates at the near Infrared frequencies; it is characterized by the usage of a narrow spectrum laser which ensure high speed data communication over long distances, ultra high bandwidth, ultra low latency and relative cheaper costs with respect to the conventional radio frequency links. This type of communication can be used for many purposes like security, video surveillance, last mile solutions and building-to-building communication. However this technology has some disadvantages like absorption and scattering by particles

[1]IDATE DigiWorld (formerly the Institut de l'audiovisuel et des télécommunications en Europe) is one of Europe's policy institute on the digital economy whose aim is to assist members and clients in the media, internet and telecommunications sectors in their decision-making.

and atmospheric turbulence which affect the optical beam propagation along the FSO link in time-spatial domain. Turbulent motions in the atmosphere generate areas with different refractive index leading to an distorted incident wavefront with a consequent loss of image quality on the detector or a low efficiency in fiber coupling in the case of optical communications. Already in the 50's astronomers were looking for a solution to this serious problem; in fact in the years to come they developed what is called adaptive optics, a system capable of correcting turbulence through the use of large deformable mirrors. This technique can also be used on FSO communication systems. In this case, since small apertures are used, it is sufficient to correct only for Tip and Tilt making the system even simpler and cheaper. This thesis work is focused on the development and tests of a refractive deformable element able to correct the beam for Tip and Tilt (Tip-Tilt Lens) in such a way that it can be easily integrated into an FSO telecommunications system to improve their performances; in particular bring a significant improvement on the fiber coupling efficiency. In Chapter 1 it is proposed an overview on atmospheric turbulence and the concept of seeing analyzing their main parameters. In Chapter 2 Adaptive Optics systems is introduced with the description of the main components and then a brief analysis on the state of the art of FSO communications is reported. The Chapter 3 is reserved for the description of the deformable lens developed in this project and its properties characterization. Finally in Chapter 4 is proposed the experiment carried out in the laboratories of CNR-IFN to test the lens; a 20 m FSO transmission of a collimated laser was performed between two telescope mounts. The beam has been focused and injected into a multi-mode optical fiber with the Tip and Tilt correction performed by the T-T lens B in closed loop.

Chapter 1

Atmospheric aberrations

1.1 Atmospheric turbulence

The atmosphere is, as a first approximation, a viscous fluid with inhomogeneous density, pressure and temperature. When light travels through the atmosphere encounters zones with different refractive indexes, consequently the original wavefront is distorted. When looking at stars or in laser communication this phenomenon leads to worse defined images or communication inefficiencies. It is possible to consider two types of fluid flow: laminar and turbulent. The laminar one is characterized by low velocities and by layers of fluid flowing parallel to each other; the turbulent flow is, instead, characterized by the presence of swirling structures. The transition between these two regimes is regulated by the ***Reynolds number***:

$$R_e = \frac{Lv}{\nu} \tag{1.1}$$

where v is the fluid velocity, in this case the wind velocity, L is the scale length and ν is the kinematic viscosity. Laminar regimes are characterized by low Reynolds numbers while turbulent regimes by high Reynolds numbers. Usually the transition value is around 2000 but it depends on the particular system which is considered. The regime of the earth atmosphere has a Reynolds number of about 10^6 and is definitely turbulent. To understand how turbulence is generated in the atmosphere, it is useful to introduce the *Kolmogorov theory.*

1.1.1 Kolmogorov theory

Once the Reynolds critical value is surpassed, the turbulent flow produces eddies which dissipate energy dividing into smaller ones through a cascade

mechanism as reported in Fig. 1.1. This process occurs in a precise regime, called *Inertial regime*, included between the *outer spatial dimension* L_0 and the *inner spatial dimension* l_0 where the viscous effects are no more negligible.

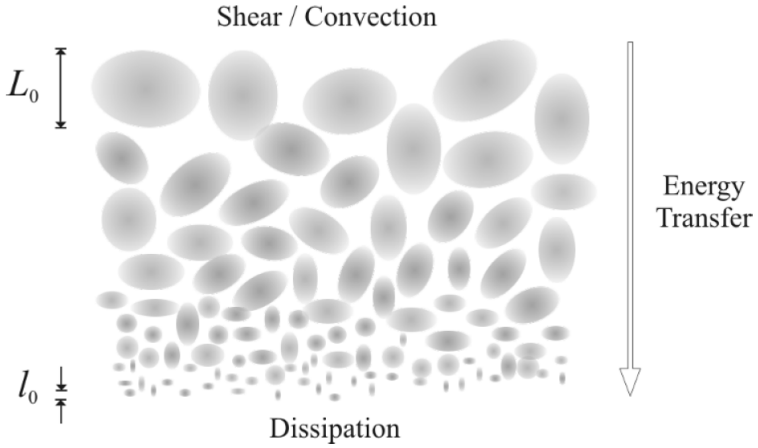

Figure 1.1: Cascade mechanism of the energy dissipation on atmospheric turbulence.

The Kolmogorov theory describes the energy spectrum of the turbulence and is based, inside the inertial regime, on three principal hypotesis: the fluid, in this case the atmosphere, must be locally *omogeneus, isotropic and incompressible*. The spectrum diagram is reported (see Fig. 1.2).

Considering the previous assumptions, the structure function, which describes the turbulence, is derived from the *Navier-Stokes equations*:

$$D_v = C_v^2 \cdot |R_1 - R_2|^{\frac{2}{3}} \tag{1.2}$$

where R_1 and R_2 are the positions of two considered points and C_v^2 is the *velocity structural parameter*, in other words it measures the amount of kinetic energy of the turbulence. The same quantity can be expressed using the refractive index n (35), a more suitable parameter to describe the atmospheric aberrations:

$$D_n = C_n^2 \cdot |R_1 - R_2|^{\frac{2}{3}} \tag{1.3}$$

where C_n^2 is the *refractive index structural parameter* which describe the local variation of n. It can be described in function of the altitude h as follow:

$$C_n^2 = 5.94 \cdot 10^{-23} h^{10} \left(\frac{W}{27}\right)^2 e^{-h} + 2.7 \cdot 10^{-16} e^{-2h/3} + A e^{-10h} \tag{1.4}$$

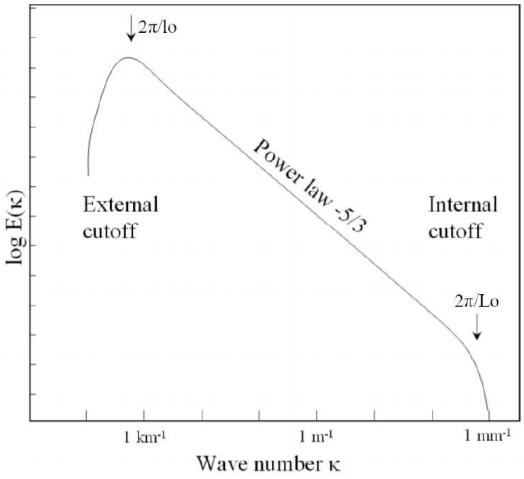

Figure 1.2: Energy spectrum of the turbulence where the external and internal cutoff are respectively at $2\pi/l_0$ and $2\pi/L_o$ (9).

where h is expressed in kilometers, A and W are two parameters which depend on the wavelength and can be adjusted for local conditions. The vertical distribution of the refractive index structural parameter is fundamental to describe the aberration suffered by the wavefront and the effect that it produces on the images, known as *Seeing*.

1.2 Seeing

When the wave enters the Earth's atmosphere, the plane wave is distorted because the index of refraction is not uniform. The resulting wavefront is no longer flat but aberrated. The seeing is the measure of this aberration effects on the light due to atmospheric inhomogeneities. In principal, the resolution of an optical system can be limited by many factors such as misalignments or imperfections on optical elements; in any case a theoretical limit is imposed by the diffraction which makes an optical system *diffraction limited*. In case of a circular aperture, the pattern of a point like source through a diffraction limited system is known as *Airy pattern*. As said before, when we are observing the sky or we are performing telecommunications, the system is no longer limited only by the diffraction but we have to consider the presence of the atmosphere, in this case the system is *seeing limited*. The image of a seeing limited system is known as *speckle image* and is reported in Fig. 1.3 (5) with a comparison of two images, one seeing limited and one diffraction limited.

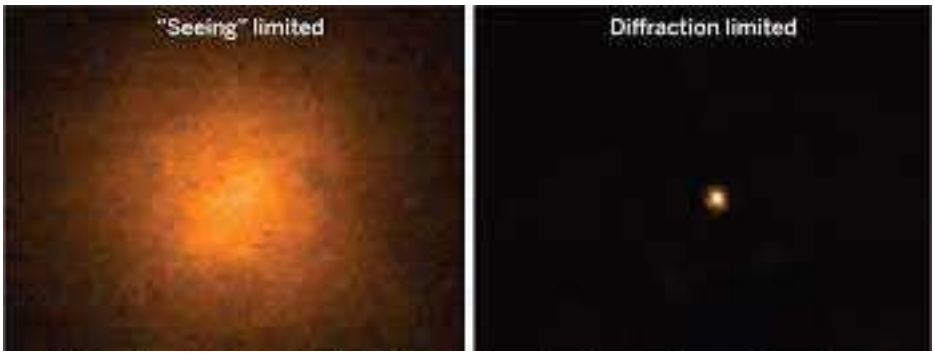

Figure 1.3: Comparison of the same image with two different system, on the left using a seeing limited system and on the right side with a diffraction limited system, (5).

It is, now, useful to introduce some parameters that can be considered as an estimate of the seeing; each of them is function of the C_n^2:

- **The Fried parameter (r_0)**: it defines the aperture beyond which the root mean square of phase aberration is more than one radian; it also represents the size of the turbulent cells in the atmosphere. It is defined as follow:

$$r_0 = \left[0.423k^2 \sec\beta \int_{Path} C_n^2(z)dz\right]^{-\frac{3}{5}} \tag{1.5}$$

  where β is the zenith angle, k is the wave number, z is the vertical coordinate and the integral is calculated along the optical path. If we consider $k = 2\pi/\lambda$ it is not difficult to describe the Fried parameter in terms of λ:

$$r_o \propto (\lambda^{-2})^{-3/5} \propto \lambda^{6/5} \tag{1.6}$$

  If the telescope aperture D is larger than r_0 the system is to be considered seeing limited. Typical values of r_0 in visible range are 10-20 cm.

- **The isoplanatic angle (θ_0)**: it defines the angular size beyond which the RMS of phase aberration is more than one radian. It is defined as follow:

$$\theta_0 = \left[2.91k^2 \sec^{8/3}\beta \int_{Path} C_n^2(z)z^{5/3}dz\right]^{-\frac{3}{5}} \tag{1.7}$$

  The isoplanatic angle determines the area on the sky within which the aberration can be considered quite similar for all the objects. Therefore the reference star for an adaptive optics system has to be chosen inside

this area, otherwise its aberrations would be so different from those of the observed object that the system would not perform effectively.

- **Full Width at Half Maximum**: is the product of the time integration of all the wavefront aberrations, it is defined as follow:

$$FWHM \approx 5.6\lambda^{-1/5}\left(\frac{1}{\cos\beta}\int C_n^2(z)dz\right)^{3/5} \approx 1.035\frac{\lambda}{r_0} \tag{1.8}$$

In addition to these indicators it is important to consider, also, the following important parameter:

- **The coherence time** (τ_0): it defines the temporal statistic of the aberration which can be described both by the wind velocity or by the evolution of the eddies. The best description of this parameter can be obtained with the *Taylor's hypothesis* which assumes that the variation timescale of the turbulent cells is much greater than the time spent by the wind to "slide" the cells through the aperture. In this case we can consider that the temporal evolution of the aberration, that should correspond to the correction speed of the AO system, derives from the passage of "frozen" eddies. τ_0 depends on r_0 and it is defined as follow:

$$\tau_0 = 0.314\frac{r_0}{v} \propto \lambda^{\frac{6}{5}} \tag{1.9}$$

where v is the wind velocity. From NOAA (12), the average value of the wind velocity in the state of New York on july 2021 was 5 m/s^{-1}, with typical values of r_0 we obtain a value for τ_0 of few millisecond; this value is fundamental for the AO system because it gives an estimate of the required correction frequency. From τ_0 we can retrieve *the Greenwood frequency* $f_g = 1/\tau_0$ that describe the frequency related to the turbulence change.

The atmospheric turbulence produces two main effects:

- **Scintillation**: scintillation is an effect, visible even to the naked eye, which results in a variation of the received intensity of point like sources. The turbulent cells on atmosphere create both convergence and divergence effects on the wavefront, leading to interference. It depends on the pupil aperture and on the altitude of the turbulent layer, the higher it is the more the effects is amplified. This phenomenon does not act on extended object because we can see them as a series of point like sources whose scintillation effects compensate each other.

- **Tip-Tilt**: tip and tilt are low order aberrations and describe the angular deviation of the wavefront produced by the turbulence. The angular displacement observed of a star in the sky with a telescope of aperture D (36) is :

$$\alpha = \sqrt{0.18 \cdot \left(\frac{D}{r_0}\right)^{5/3} \left(\frac{\lambda}{D}\right)^2} \tag{1.10}$$

  Tip-tilt becomes important for aperture comparable with the dimension of the turbulent cell or, in other words, with the value of r_0.

1.3 Strehl ratio

As mentioned above, in absence of aberration the resolution of a telescope is limited only by the diffraction. This phenomenon is generated when a beam of light is partially blocked by an obstacle, in this case some light is scattered around that object creating light and dark bands. Considering the two dimensional case of a circular aperture and incoming plane wave (telescope case), the radiation pattern is described by:

$$I(\alpha) = I_0 \left(\frac{2J_1(ka \sin \alpha)}{ka \sin \alpha} \right)^2 = I_0 \left(\frac{J_1(x)}{x} \right)^2 \tag{1.11}$$

where I_0 is the maximum intensity on the center, α is the angle on the image plane, J_1 is the Bessel function at first order, k is the wave number and a is the aperture radius. This equation describes the pattern known as *Airy pattern*, reported in Fig. 1.4, which, in the case of a telescope, represents also the *Point spread function* (PSF) in absence of aberration.
Considering that the first zeros of the Bessel function J_1 is at:

$$x = ka \sin \alpha = 3.8317 \tag{1.12}$$

we found that the angle at which is located the first minimum of intensity is:

$$\sin \alpha = \frac{3.8317}{ka} = \frac{3.8317\lambda}{2\pi a} = 1.22 \frac{\lambda}{D} \tag{1.13}$$

where D is the telescope aperture. This equation describe the angular resolution of a telescope without aberration. In presence of aberrations, of course, the PSF is described by a distorted pattern with a consequent reduction of the maximum intensity. The Strehl ratio S is defined as the ratio between the maximum intensity of the observed PSF and the peak intensity of a diffraction limited PSF, the *Airy disk*. This parameter is dimensionless with

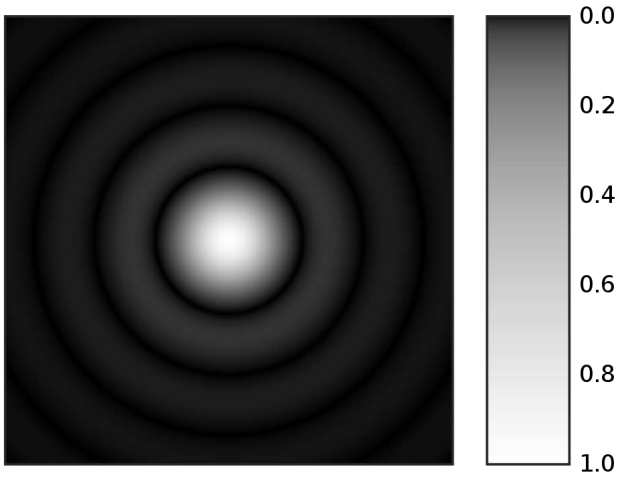

Figure 1.4: Airy disk representation with intensity scale (Author: Sakarumbo)

values ranging from 0 to 1, it measures the quality of the wavefront after the propagation through the turbulent layers. From the comparison of the Strehl ratios of the corrected and uncorrected image it is possible to retrieve the quality of the correction. It has assumed an important role also in industry to summarize the performance of an optical system. Considering a circular aperture and an aberration function in polar coordinate $\phi(\rho, \theta)$, S is given by:

$$S = \frac{1}{\pi^2}\left|\int_0^1 \int_0^{2\pi} e^{ik\phi(\rho,\theta)}\ d\rho\ d\theta\right|^2 \tag{1.14}$$

where S= 1 when the wavefront is not perturbed and S<< 1 for high variation of ϕ. If RMS phase aberration σ is less than 2 radians, in Kolmogorov theory the *Strehl ratio* can be written as:

$$S \approx e^{-\sigma^2} \tag{1.15}$$

$$\sigma^2 = 1.03\left(\frac{D}{r_0}\right)^{5/3} \tag{1.16}$$

where it easy to observe that for $D = r_0$ the *Strehl ratio* is $S \approx 0.36$.

1.4 Wavefront representation with Zernike polynomials

To describe and evaluate the incoming wavefront is useful to represent it with a polynomial decomposition known as *Zernike decomposition*. Zernike polynomials are orthogonals on a circular aperture of unit radius so it is possible to describe each single aberration in this domain with a linear combination of them. Considering a single circular aperture of unit radius, the Zernike polynomials in polar coordinate (ρ, θ) with $\theta \in \{0, 2\pi\}$ and $\rho \in \{0, 1\}$ are defined as:

$$Z_n^m(\rho,\theta) = N_n^m R_n^m \begin{cases} \cos m\theta & m \geq 0 \\ \sin m\theta & m < 0 \end{cases} \tag{1.17}$$

where N is the normalization constant:

$$N_n^m = \sqrt{\frac{2(n+1)}{1+\delta_{mn}}} \tag{1.18}$$

and R is the radial part described by:

$$R_n^m = \sum_{s=0}^{(n-m)/2} \frac{(-1)^s (n-s)!}{s![(n+m)/2-s]![(n-m)/2-s]!} r^{n-2s} \tag{1.19}$$

The m index is the so called *azimuthal frequency* and n is the *radial degree*. The RMS of phase aberration $\phi(\vec{r})$ in a unit radius aperture can be, finally, expressed with a combination of the Zernike polynomials as follow:

$$\phi(\vec{r}) = \sum_{j=1}^{\infty} a_j Z_j(\vec{r}) \tag{1.20}$$

where a_j is the aberration coefficient. In Fig. 1.5 are reported the first 15 *Zernike modes*, with the representation of each single aberration. To evaluate how an adaptive optics system corrects the incoming wavefront it is possible to consider the *residual errors* after the loop correction. The first one is related to the adaptive element that introduces error when it tries to reproduce the opposite of the aberration (*Fitting error*), a second one rises because the adaptive element cannot respond instantaneously to the aberration (*Temporal error*), the next is due to the different position of the source used for the wavefront measurement (*Isoplanatic error*) and, finally, the last one is related to sensor noise (*Sensor noise error*). The sum of them determine the total RMS phase aberration σ_T^2:

$$\sigma_T^2 = \sigma_{Isoplanatic}^2 + \sigma_{Fitting}^2 + \sigma_{Temporal}^2 + \sigma_{Noise}^2 \tag{1.21}$$

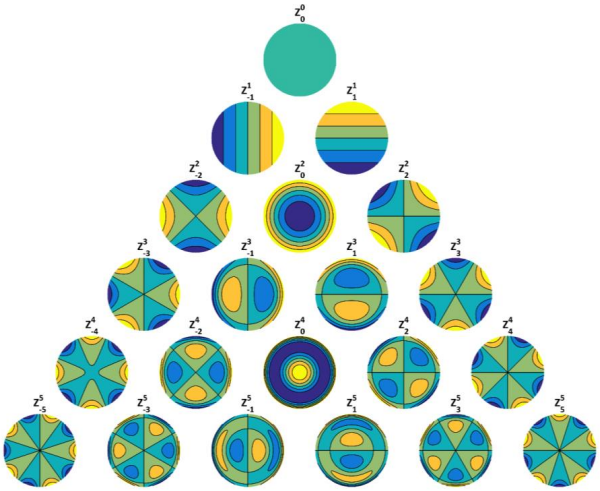

Figure 1.5: Representation of the first 15 Zernike modes (27).

Once the correction is performed, it is interesting to know how much wavefront aberration remains; also because it can be an indicator of how important it is to correct certain aberrations rather than others. Noll (25), reported that, once the first J Zernike modes are removed it is possible to calculate the residual wavefront error Δ_j as follow:

$$\Delta_j = \langle \phi^2 \rangle - \sum_{j=1}^{J} \langle |a_j|^2 \rangle \tag{1.22}$$

the first values of Δ_j are shown below:

- **Piston** $= \Delta_1 = 1.0299(D/r_0)^{5/3}$
- **Tip** $= \Delta_2 = 0.582(D/r_0)^{5/3}$
- **Tilt**$= \Delta_3 = 0.134(D/r_0)^{5/3}$
- **Defocus** $= \Delta_4 = 0.111(D/r_0)^{5/3}$
- **X Astigmatism** $= \Delta_5 = 0.088(D/r_0)^{5/3}$
- **Y Astigmatism** $= \Delta_6 = 0.0648(D/r_0)^{5/3}$

if J is large (> 10) the expression can be approximated by:

$$\Delta_j \approx 0.2944 J^{-\sqrt{3}/2} \left(\frac{D}{r_0}\right)^{5/3} [rad^2] \tag{1.23}$$

We can observe that correcting the wavefront only for Tip and Tilt, as in our experiment, it is possible to reach a residual error of $\Delta_3 = 0.134(D/r_0)^{5/3}$; so Tip and Tilt represent a consistent part, in particular about the 87%, of the total wavefront aberration, mostly for small aperture telescopes. A representative diagram of the residual error in function of the corrected Zernike modes N can be obtained from the previous equations; following it is reported using a fixed ratio $(D/r_0) = 0.9$ *(Small aperture)*.

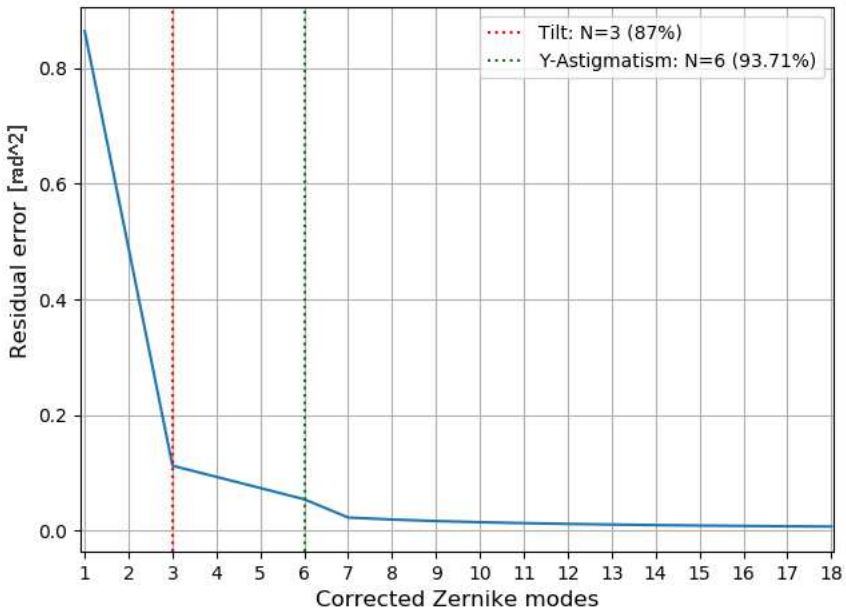

Figure 1.6: Residual error in function of the corrected Zernike modes N. The dotted lines indicate the percentage of corrected error for the first N modes (in this case are reported the case of Tilt and Y-Astigmatism).

This graph is useful in our case because it gives an idea of the residual error after correcting for Tip and Tilt using the deformable lens that will be introduced in Chapter 3.

Chapter 2

Adaptive optics systems

Adaptive optics systems (AO) have been developed in astronomy to correct the wavefront aberration in order to reach a better image quality. The first solution was proposed by Horace Babcock in 1953 (2); he explained how the atmospheric aberration can be corrected using a particular adaptive mirror guided by a feedback sensor. Due to several system limitations and to prohibitive costs the project was temporarily shelved. This concept was recovered and developed by the *US Department of Defense*, during the Cold War, to improve their Soviet satellite tracking system compensating the atmospheric distorsions. The first working AO system was designed by Hardy at the end of 70's and installed in 1982 at Air-Force Maui Optical site. In astronomy, the first prototype was the "COME-ON" developed by European Southern Observatory (ESO) (22) then udpdated in "COME-ON+".

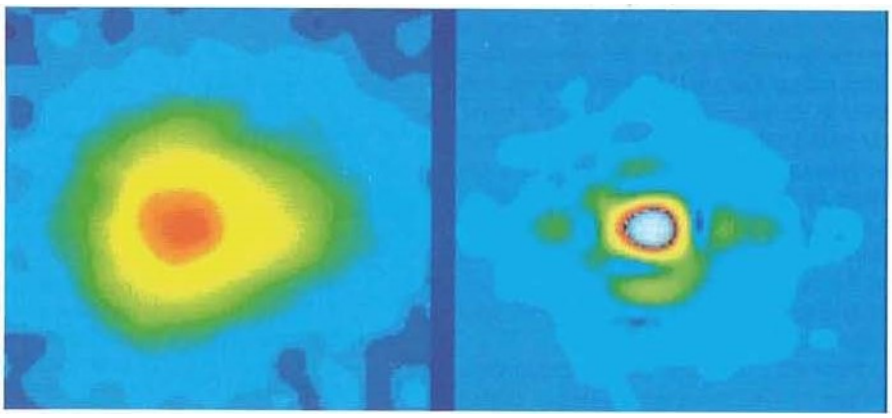

Figure 2.1: Imaging of Deneb taken with COME-ON system in 1989 (22). It is possbile to observe the difference between the non corrected image (left) and the corrected one (right).

An AO system is a real-time distortion-compensating system which tries to correct the optical path variations by measuring the wavefront aberration using a feedback element. The principal AO system components, reported in Fig. 2.2, are:

- **Wavefront Sensor**
- **Deformable element (mirror, lens)**
- **Wavefront reconstuctor and Controller**

The *Wavefront sensor* measures the aberration of the system; a control computer evaluates the sensor measurement to send input signal to the *Deformable elements* which can change its surface to compensate the light distortions measured by the wavefront sensor itself. The control can be performed in *Closed loop* or in *Open loop*. In an open loop system the wavefront sensor is placed before the deformable element, therefore there is no feedback (see red loop in Fig 2.2). In a closed loop system the wavefront sensor is placed after the deformable mirror and the correction is performed on the basis of the difference between the aimed wavefront phase and the mesured one (see blue loop in Fig 2.2).

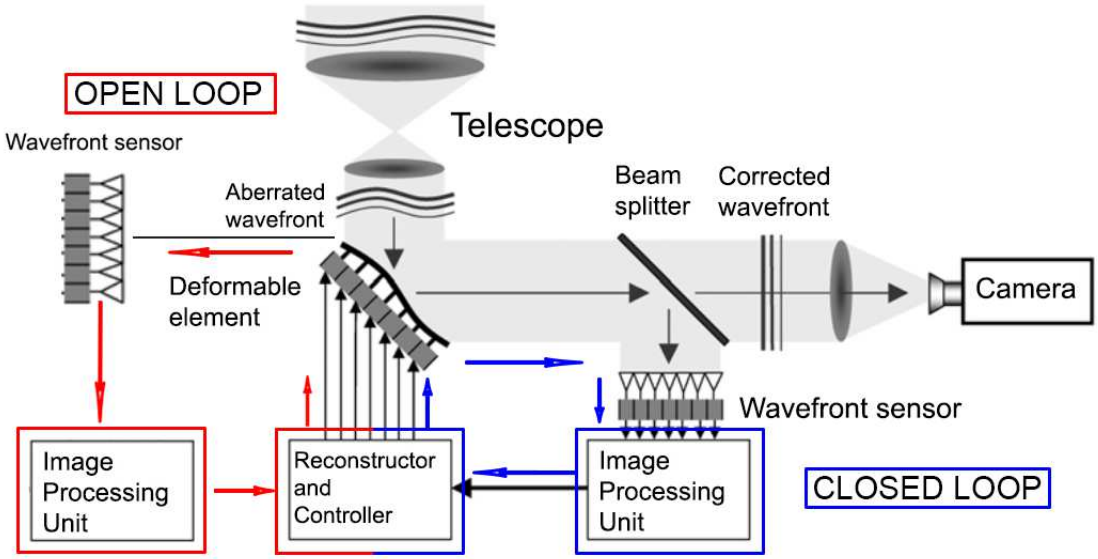

Figure 2.2: Example of an AO system (39).

2.1 Wavefront sensor

There are 4 main types of WFS used to correct different kinds of aberrations:

- **Tip-Tilt WFS's:**
  - Quad Cell Wavefront Sensor
- **High order aberrations WFS's:**
  - Shack-Hartmann Wavefront Sensor
  - Curvature Wavefront Sensor
  - Pyramid Wavefront Sensor

2.1.1 Quad Cell Wavefront Sensor

The Quad Cell WaveFront Sensor (QC WFS) is the simplest type of sensor and it is used to evaluate the tip-tilt of the wavefront. Theoretically is composed by 4 sensors but it can be reproduced by a single camera divided virtually in four parts. It is placed near the focal plane and it evaluates the spot displacement, on x and y axis, measuring the energy difference of the four zones as follows:

$$S_x = \frac{(B+D)-(A+C)}{A+B+C+D} \tag{2.1}$$

$$S_y = \frac{(A+B)-(C+D)}{A+B+C+D} \tag{2.2}$$

where S_x and S_y are proportional to the wavefront first derivative and A,B,C,D are the intensities on the four quadrant of the sensor represented in Fig. 2.3. To determine Tip-Tilt is necessary to consider the linear growth range of

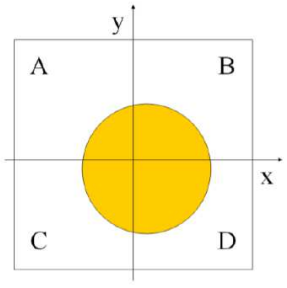

Figure 2.3: Representation of the Quad Cell WFS (9).

S_x (S_y), reported in Fig. 2.4, that is when the spot is detected by all the four quadrant; it depends also on the spot size, indeed it is useful to find the suitable size of the spot in order to reduce the saturation part and to increase the sensitivity.

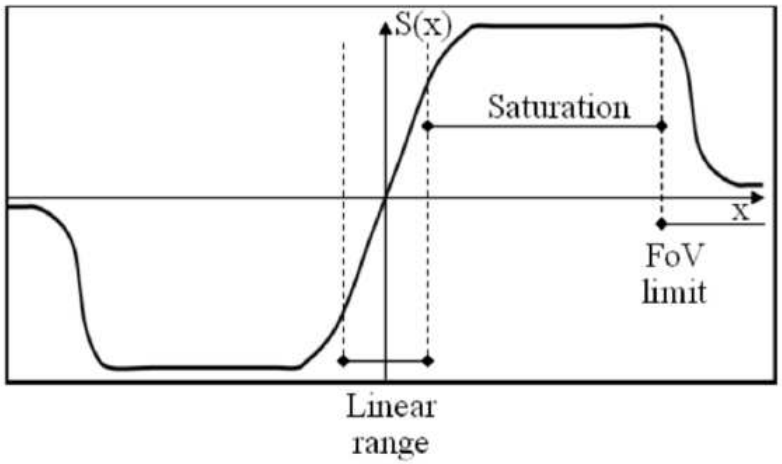

Figure 2.4: S_x signal profile in function of x (9). It is possible to see the linear range useful to determine the Tip-Tilt effect.

2.1.2 Shack-Hartmann Wavefront Sensor

The Shack-Hartmann WaveFront Sensor (S-H WFS) is based on the *Hartmann optical testing technique*; it consists in positioning a mask, with a fixed number of sub-apertures, over the telescope aperture. It permits to sample a small area of the total aperture for each hole present in the mask, in this way it is possible to analyze the beam with higher precision in order to retrieve higher order aberrations. This method, however, had the disadvantage of losing a significant amount of light. To solve this problem it has been introduced the Shack-Hartmann WFS which replaces the mask with a lenslet array, in this way all the flux is collected. The array is positioned on the pupil plane and the detector is placed on the focal plane. To increase the sampling precision of the sensor could be useful to have a large number of lenses $N = D/d$, where D is the beam size and d is the lens size; The S-H WFS measures, dividing the beam in smaller portions, the local inclination of the wavefront. As reported in Fig. 2.5, if the wavefront has non aberration the spots are equally spaced. Instead, if the wavefront presents some distortion, each lens focuses her portion of the beam in a slightly different position.

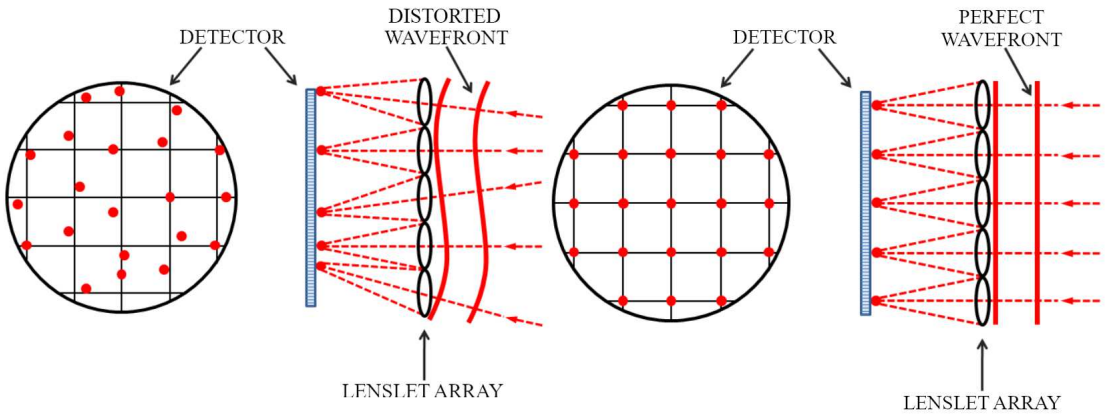

Figure 2.5: Representation of the S-H WFS (32). On the left side is reported the case of the aberrated wavefront and on the right side the case of the corrected one.

Assuming a QC WFS for each sub-aperture and small displacement on the detector, the angular displacement are described by:

$$a_x = \frac{\lambda}{2d}\frac{(A+C)-(B+D)}{A+B+C+D} \tag{2.3}$$

$$a_y = \frac{\lambda}{2d}\frac{(A+B)-(C+D)}{A+B+C+D} \tag{2.4}$$

The associated error to the S-H WFS, in particular the uncertainty related to the position of the spot, depends on the number of collected photons M as follow:

$$\epsilon_{SH} = \frac{\lambda}{r_0}\frac{1}{2\sqrt{M}} \tag{2.5}$$

2.1.3 Curvature Wavefront Sensor

Invented by F.Roddier, this sensor measures the curvature of the wavefront ($\nabla^2\phi(\vec{r})$) taking two images of the source, one in an intra-focal position and one in an extra-focal position. If the wavefront is aberrated, there is a disuniformity on the intensity of the two images, as shown in Fig. 2.6; in particular, a positive curvature of the WF produces a more intense intra-focal image with respect to the extra-focal one. The normalized difference of the intensity related to the two planes ($I_1(\vec{r}), I_2(\vec{r})$) is proportional to the second derivative of the wavefront as follow:

$$\frac{I_1(\vec{r})-I_2(\vec{r})}{I_1(\vec{r})+I_2(\vec{r})} = C\left[\nabla^2\phi(\vec{r}) - \frac{\partial\phi(\vec{r})}{\partial\vec{n}}\right] \tag{2.6}$$

where C is the proportionality constant.

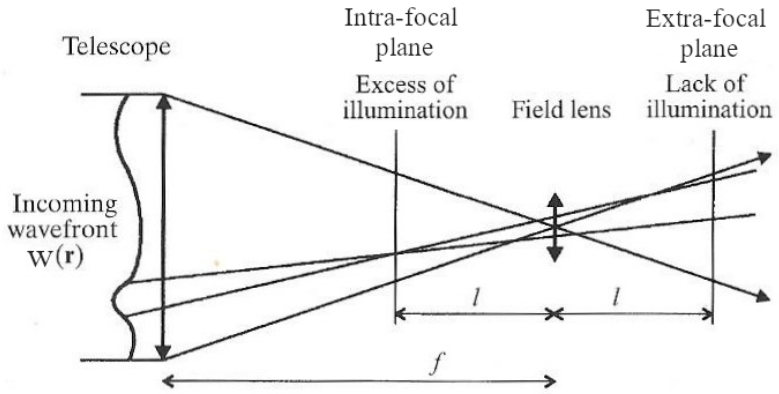

Figure 2.6: Scheme of the curvature WFS where l is the distance from the two plane to the focus, f is the focal length and W(r), in this case, is the wavefront (30).

2.1.4 Pyramid Wavefront Sensor

Invented by R.Ragazzoni (28), this sensor is able to detect high order aberrations by using a square-based pyramidal prism whose vertex is located in the focal plane. As reported in Fig. 2.7 the light is divided into four beams by the four prism faces, each of these produces a different image of the pupil whose intensity is proportional to the amount of light hitting each quadrant. Tip-tilt is measured with the same method of the QC WFS, reported in equation (2.1) where A,B,C and D, in this case, are the fluxes of the four different pupil images. Similar to the T-T analysis, high order aberrations are determined considering the difference in flux of the same sub-aperture taken from each pupil image (see Fig. 2.8).This sensor has some pros with respect to the S-H WFS, some examples are given below:

- *Poissonian error reduction*: $\epsilon_p = \frac{\epsilon_{SH}}{N}$ where ϵ_{SH} is the error associated to the S-H WFS and N is the number of lenses in the array.

- *More sensitivity in Closed loop*: Decreasing of the spot size on the vertex causes an increase in sensitivity and a consequent increase in the signal to noise ratio (SNR).

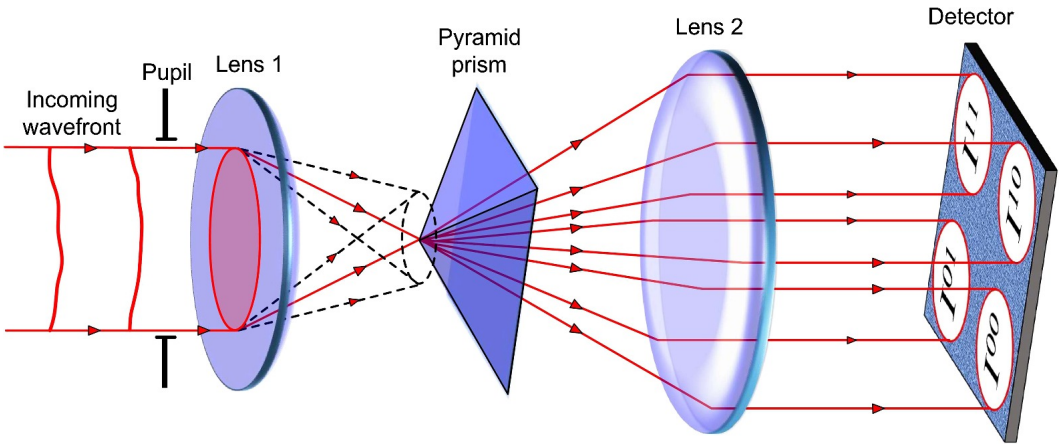

Figure 2.7: Operating scheme of the pyramid WFS.

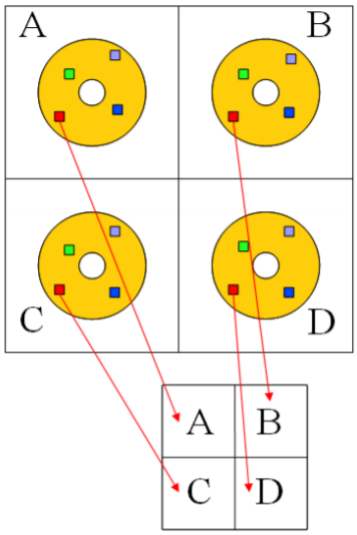

Figure 2.8: High order aberrations analysis with the pyramid WFS (9).

2.2 Adaptive elements

These elements are able to correct the wavefront aberration using instructions from the control system. They are, in general, composed by an array of actuators connected to an optical surface which can deform its shape. The main parameters which describe a deformable element are:

- ***Number of actuators:*** It describes the degrees of freedom that the system can correct.
- ***Response time:*** It is the time it takes for adaptive element to execute

the controller's instructions. It is an indicator of the frequency at which these devices work.

- ***Stroke:*** It is the maximum extension of the actuators from its reference position.
- ***Actuators position***

The main types of deformable elements are described below:

- *Spatial Light Modulators (SLM)*: SLMs are devices used to modulate phase, intensity, direction and polarization of the incoming light. There are two main types of SLMs:
  - *EASLM (Electrically Addressed SLM):* Images are created and controlled electronically (es: electronic display).
  - *OASLM (Optically Addressed SLM):* The image, in this case, is created and changed by shining light encoded with an image on its front or back surface.

  SLMs have, in general, an high spatial resolution and high working frequency.
- *Deformable Mirrors (DM)*: These elements are characterized by a mirror surface deformed by actuators. The first type of DM in astronomy was the segmented DM, they are formed by a series of mirror controlled separately with same shape and dimension; each piece in general has 3 degree of freedom (piston, tip and tilt). For smaller aperture it can be used a continuous surface DM. Piezoelectric actuators and electromagnetic actuars are the most commonly used actuators for deformable mirrors. The use of deformable mirrors into existent optical system is not so practical, it necessitates the creation of folded optical paths; for this reason the application of refractive wavefront correctors like deformable lenses can be useful.
- *Deformable Lenses (DL)*: DL are refractive devices which can correct, in principal, few optical aberrations. There are several type of existing DL with different actuators and smart materials, but, in general, they cannot correct for high order aberrations. The device that we will introduce on the next chapter is included in this category, a lens that can correct only up to Tip and Tilt distortion. To reach high order deformation Stefano Bonora et al. proposed a Multi-actuator Adaptive Lens (MAL) that can correct up to the 4th order aberration (3). This

lens, for example, is composed by thin glass layer which space between them is filled with a transparent mineral oil. The shape is controlled by a piezoelectric actuator ring for each surface. A significant advantage of deformable lenses is that they can be easily introduced on a wide range of existing optical system without change the configuration.

In Fig. 2.9 is reported the difference between the integration of a DM and a DL in an existing system.

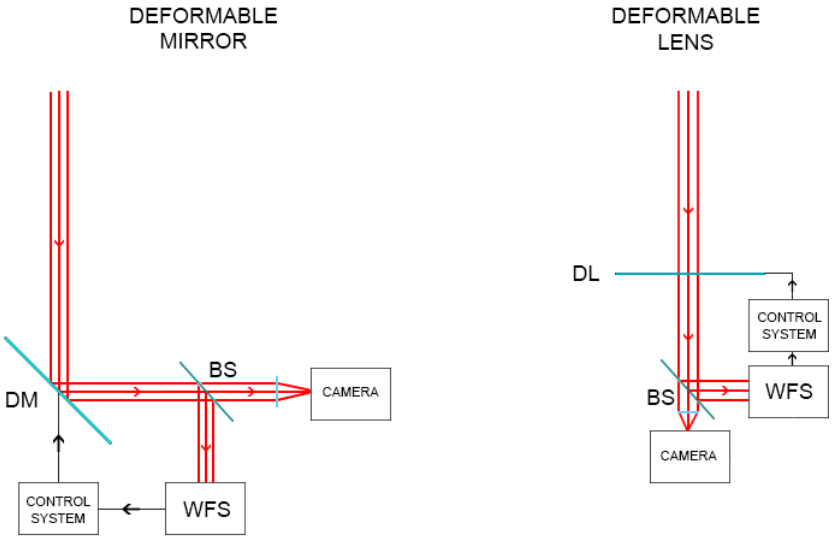

Figure 2.9: As can be seen the adaptive lens is more easily inserted in the optical path. This is particularly important when working with pre-existing systems or to implement compact systems..

The choice of actuators in an AO system is not obvious, there are many types of actuators based on different technologies. In our case piezoelectric actuators have been chosen, a full description is given in the next section.

2.2.1 Piezoelectric actuators

The piezoelectric effect is the ability of certain materials to generate an electric charge in response to applied mechanical stress, this is known as *direct piezoelectric phenomenon*. It is possible to generate a mechanical deformation on the material using a certain voltage, in this case it is known as *converse piezoelectric phenomenon*. In general, the converse effect is more used for actuating technology, as in our case. The direct and converse effects of piezoelectric materials are achieved by a *poiling* process, which involves

exposing the material to high temperatures while imposing high electric field intensity in a desired direction; in this way the dipoles inside the material reorientate along the poling axis. This effect is the basis of piezoelectric actuators; if we consider a disk actuator (30), reported in Fig. 2.10a, with thickness e, a longitudinal electric field E can change the relative thickness $\Delta e/e$ to:

$$\frac{\Delta e}{e} = d_{33}E \tag{2.7}$$

where d_{33} is the longitudinal piezoelectric coefficient. Introducing the voltage V=Ee

$$\Delta e = d_{33}V \tag{2.8}$$

To obtain a substantial deformation, a single disk actuators is not enough. It is possible to use the so called *piezo stack actuator*, reported in Fig. 2.10b, i.e. arranging multiple layers of piezoelectric materials on top of each other. In this way, putting many pieces together creates a multiplicative effect on their transformations magnitude for the same voltage, amplifying their power.

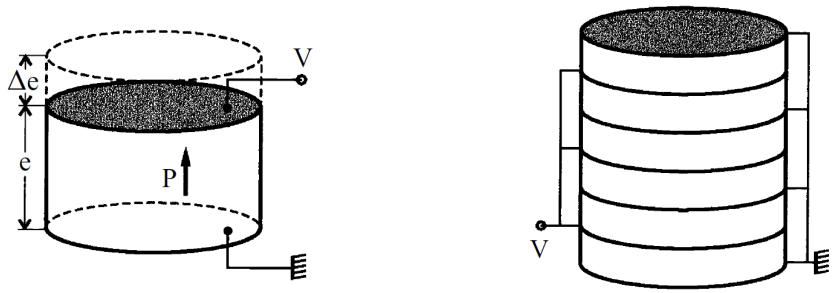

(a) Single disk actuator

(b) Piezo stack actuator

Figure 2.10: Difference between a single disk actuator and a piezo stack actuator (30).

Piezoelectric actuators exhibit a field–strain relation which causes a significant hysteresis behaviour. The hysteretic beahviour of the piezoelectric materials means that the strain reached with a certain applied voltage depends not only on the actual value but also from the past values assumed. In Fig. 2.11 a theoretical hysteresis cycle is proposed; it is possible to see that for the same value of the electric field we have two or more values of the position (remember that, without hysteresis, for one value of E should be correspond a single value of the position). On the next chapter it will be explained how we calculated the hysteresis cycle of our piezoelectric actuators.

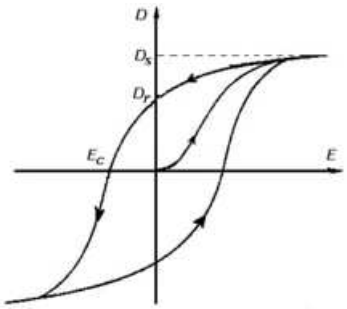

Figure 2.11: Theoretical hysteresis cycle. The x-axis is the electric field E while the y-axis is, in this case, the deformation of the piezoelectric material.

2.2.2 Magnetic Actuators

The magnetic actuation is based on the magnetic effects to generate a displacement on a mechanical structure. There are two main families of magnetic actuators whose difference is based on the technology leveraged. The first one is based on the Lorentz force and the reluctance force and can be compared with piezoelectric actuators; they are sorted in three groups:

- *Moving coil actuators*: Actuators are in a static magnetic field where a mobile coil is driven by a current. In this way actuators are controllable.
- *Moving magnet actuators*: Actuators, in this case, are between two magnet poles where a mobile permanent magnet can be switched from on pole to the other. This type of actuators is bi-stable.
- *Moving iron actuators*: They are based on the reluctance force.

The second family is based on magnetically-controlled active materials, materials that change their shapes when exposed to magnetic fields. An example is a nickel rod that tends to deform when it is placed in an external magnetic field. Magnetic actuators has some advantages like high actuation force and stroke, contactless remote actuation and low voltage actuation; on the other side it bring with them disadvantages like high power dissipation and fabrication of the coil.

2.3 Calibration and control

The calibration of an AO system sets the zernike modes of the deformable element and represents a fundamental step to correct aberration. It consists, in

general, in measuring the wavefront during the actuators movements. What it has to be obtained is a relation between the phase $\vec{\phi}$ of the wavefront and the vector $\vec{c}$ with the commands for the adaptive element:

$$\vec{\phi} = \mathbf{A}\vec{c} \tag{2.9}$$

where $\mathbf{A}$ is the so called influence matrix. To form the matrix you need to move the actuators separately in order to register the wavefront $\vec{\phi}$ response for each vector $\vec{c}$, each actuator fill a column of the matrix. Vectors $\vec{c}$ has the same dimension of the number of actuators. Now, to control the deformable element, what we want to do is to invert the influence matrix $\mathbf{A}$. If $\vec{\phi}$ and $\vec{c}$ have the same dimension, i.e the system is so called *determined*, the inversion should not be so difficult; but inverting a square matrix is possible only if it is not singular. Singular, in this case, means that there are some groups of actuator commands that recreate the same sensor signals with multiple combinations. This fact is basically always present so the matrix cannot be inverted; using the least squares method is possible to obtain a solution $\mathbf{K}$ known as the *pseudoinverse of* $\boldsymbol{A}$. This matrix, in optics, is called *reconstruction matrix* and it is defined as follow:

$$\mathbf{K} = (\mathbf{A}^T\mathbf{A}^{-1})\mathbf{A}^T \tag{2.10}$$

Once the modes of the adaptive elements are set, it is possible to control it, for example, in a closed loop system. From the measure of the wavefront phase at a certain time t-T, where T is the time taken from the system to complete a correction cycle, we obtain the residual error $\vec{e}(t) = \vec{\phi}_0 - \vec{\phi}(t)$. The feedback control law can be:

$$\vec{c}(t) = \vec{c}(t-T) + g\mathbf{K}\vec{e}(t-T) \tag{2.11}$$

where g is the gain of the system (generally a valuefrom 0 to 1). This type of feedback is an integrative feedback. If we consider a linear response of the system, the working frequency is $f = 1/T$. During calibration and control procedures, in our case, the wavefront has been characterized with a *modal* description, i.e. has been expressed in terms of Zernike polynomials. In Fig. 2.12 is reported a flux diagram which describes a full open loop control system. Adaptive optics systems are not only applied in astronomical environments, but can be used for multiple purposes. In particular, in this thesis work, we studied the application of a Tip-Tilt adaptive optics system for improving Free Space Optical Laser comunication efficiency.

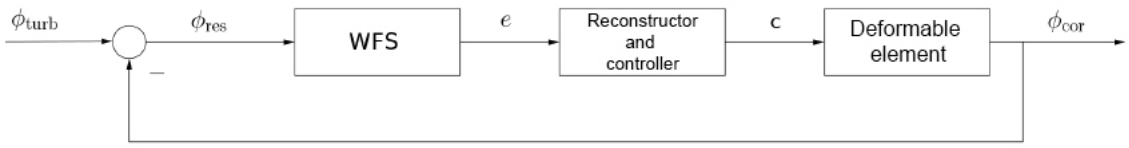

Figure 2.12: Operations of a closed loop control system.

2.4 AO in Free Space Optical Communication (FSO)

In the last years, the growth of both the high speed multimedia services and the mass volume of mobile data has led to thinking about other solutions than the most widely used *Radio Frequency* communication that is incapable to handle the enormous future data rate demands. Optical Wireless Communication (OWC) can be considered as an efficient solution thanks to his broad spectrum, ultra-high data rate, low latency, low cost and high capacity range from nanometers to several kilometers. Another important aspect to take into account of OWC is that there is no need to build a comprehensive infrastructure reducing installation costs and following an important eco-friendly view. Optical wireless communication can be divided in three main categories: OWC systems operating in the visible band are commonly known as Visual Light Communication (VLC), point-to-point OWC systems which operate at the near IR frequencies are the so called Free Space Optical systems (FSO) while systems which work in the UV part of the spectrum are referred as Ultra Violet Communication (UVC). In particular, in our case, is important to spend some words on FSO systems and the relative Adaptive Optics application. Free space optical communication refers to point-to-point wireless optical transmission through the propagation media using infrared (IR) light. We can associate multiple advantages to this technology:

- FSO systems offers ultra high bandwidth (THz) with respect to the RF communication.
- Use of a narrow spectrum laser as carrier signals that ensures high speed data communication over long distances. This involves information security, large reuse factor and no effect due to electromagnetic interference with other communications.
- Cheaper than the conventional radio frequency link because the fre-

quency band occupied is not licensed so it requires no license taxes.

- No healthy problems due to the absence of side lobes on the beam.
- Ultra-low latency and low power consumption.
- High directivity and gain of FSO antennas due to its small wavelength.

FSO systems are finding wide acceptance in cases where the end consumer, for example, cannot be reached by fiber in cable or in places where the buried fiber connectivity may be too expensive. Some interesting applications can be *interbuilding connectivity*, *broadcasting* thanks to the capacity of satisfying high quality transmission to end users, *security* against possible cyber attacks on informations, *last mile solution* for users which have no access to the FTTH (Fiber To The Home) and *video surveillance* employed in public and military safety. This technology received, also, an important attention for space communication; for example inter-satellite, satellite to ground (uplink and downlink) and deep space communication. An FSO system is composed, generally, by a *Transmitter*, a *Receiver* and an *FSO channel*; the description is briefly reported below (18):

- *FSO Transmitter*: Transmitter transforms the electrical signal to an optical signal and it modulates the laser beam to transmit or send data to the receiver through the atmosphere channel. It consists, in general, in a modulator, a driver, a light source and a beam forming mechanism like a telescope. The most commonly used optical sources are laser diode (LD) or light emitting diode (LED).
- *FSO Channel*: The propagation medium of FSO links is the atmosphere. In this type of communication (horizontal links) the most important part is the troposphere because it is where most weather phenomena occur and FSO links operate at the lower part of this layer.
- *FSO Receiver*: The receiver consists in five main parts: a telescope to collects the incoming beam, a filter for the frequency of interest, a detector like a photodiode (PD), an amplifier and a demodulator. The detector is important to have the maximum efficiency for the communication, in general it should have an high response at the selected wavelength, an high SNR and a sufficient speed of response.

In Fig. 2.13 is reported a block diagram for an horizontal communication FSO system.

It is worth talking about the main parameters that define FSO communication:

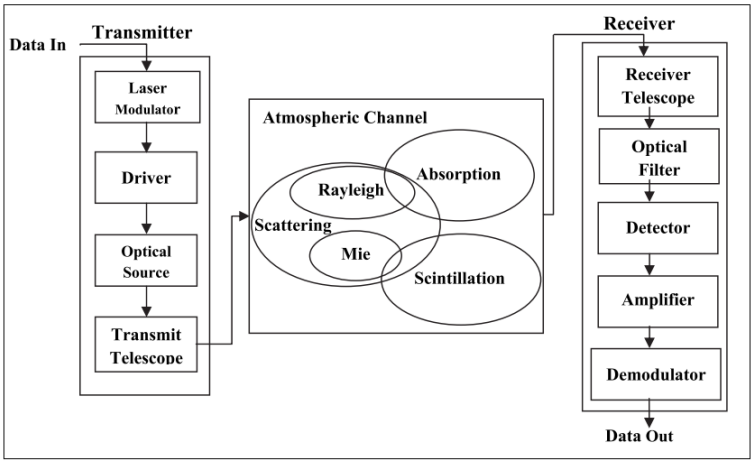

Figure 2.13: Diagram of a terrestrial communication FSO system (6).

- *Wavelength*: The selection of the best wavelength must be based on the availability of the components, eye safety, range of distance, budget and other several factors. The eye safety is one of the most important aspect to care about; the laser power depends on the spectrum range used, for example the safe laser power is 50 times larger at 1550 nm than 850 nm. The factor 50 is important because permits a propagation over long distances and support high data rates; the data rate available with commercial 850 nm systems is 622 Mbps while it possible to reach 2.5 Gbps for 1550 nm systems.

- *Beam divergence*: this feature characterizes the spreading of the beam. The beam spread depends on the beam divergence angle; if we consider a 1 mrad divergence angle we obtain a 1 m spread at a distance of 1 Km. A narrow beam in FSO system is preferred because the higher data rate and the better security.

- *Range*: The main power losses are due to the beam divergence and the scattering. Both increase with the distance between the transmitter and the receiver. For commercial use, ranges between 20-5000 m are a good choice;

- *Telescopes aperture*: The diameter aperture of the two telescopes must be adequate for the local weather condition because there is a spreading of the beam due to the atmospheric turbulence that can cause a complete loss of the signal.

FSO also brings with it important disadvantages, most of which are due to atmospheric turbulence that particularly deteriorates communication performance. Such atmospheric circulation affects the optical beam propagation along the FSO link both in time-spatial domains. Attenuation of the light is the result of absorption and scattering by molecules and particles (aerosols) suspended in the atmosphere. The bending of the beam is due to the difference in refractive index of the atmosphere. It is interesting, now, to quantify these effects on the beam power.

2.4.1 Atmospheric attenuation

The atmospheric attenuation is the partial or total loss of the incoming beam energy. It is due to multiple factors, the principal are absorption and scattering, they are briefly reported below:

- *Absorption*: The absorption process is due to the interaction of the beam photons with the aerosol dispersed particles. There are some atmospheric gases which mostly impacts on atmospheric absorption, they characterize what are called *atmospheric transmission windows*, windows of the electromagnetic spectrum where the atmosphere is transparent to certain wavelengths; in Fig. 2.14 infrared atmospheric windows are reported. The absorption coefficient β_{Abs} can be obtained from the concentration N_{Abs} and the cross section α_{Abs} of the particles in this way:

$$\beta_{Abs} = \alpha_{Abs} N_{Abs} \ [1/Km] \tag{2.12}$$

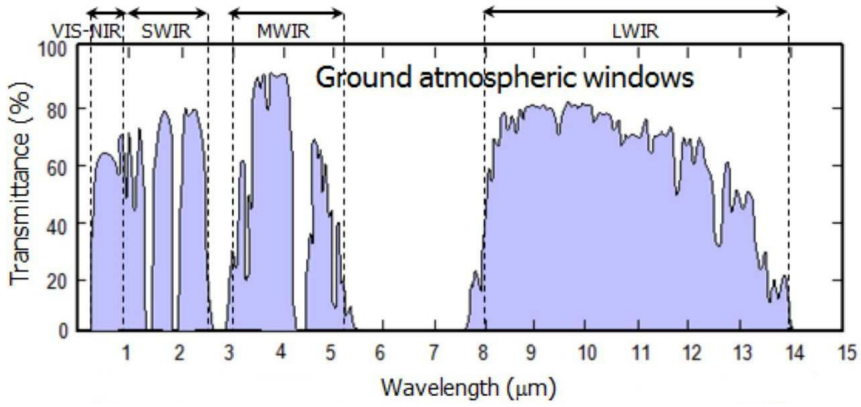

Figure 2.14: Atmospheric transmittance windows in IR (8).

- *Scattering*: is the deviation of the beam radiation into multiple directions due to the interaction of the light with the particles. There are three main types of scattering: Rayleigh scattering, Mie scattering and non-selective scattering. The difference between these three effects is due to the size of the encountered particle; the direction of the scattered light depends on the wavelength and follows a different law for each type of scattering. The total scattering coefficient β_{scat} is the sum of the Rayleigh and Mie coefficients and it is defined as follow:

$$\beta_{Scat} = \beta_R + \beta_M = \alpha_{Scat} N_{Scat} \tag{2.13}$$

  where α_{Scat} and N_{Scat} are the cross section and the concentration of the particles. The non-selective scattering is also known as *rain scattering* and is due to the interaction of the photon with the rain particles that are relatively larger than the incoming wavelength so the light can pass trough the particles; this produces a lighter effect on the beam. The coefficient in this case is calculated from the Stroke Law:

$$\beta_{RainScat} = \pi a^2 N_a Q_{scat} \tag{2.14}$$

  where a is the radius of the particles, N_a is the rain drop distribution and Q_{scat} the scattering efficiency.

Now it's possible to define the total light attenuation as the ratio of the *received power* P_r and the *transmitted power* P_t:

$$\frac{P_r}{P_t} = \frac{D_r^2}{(D_t + (\theta L))^2}\, e^{-\beta L} \tag{2.15}$$

where the free parameters D_r and D_t are the aperture sizes, θ the beam divergence and L the distance between the transmitter and the recevier. The atmosphere represents the main problem for a completely reliable FSO transmission. There are some approaches that have been tested in the past both for ground and satellite communication: *MIMO (Multi Input Multi Output)* to mitigate temporary fluctuations, *PAT (Pointing, Acquisition and Tracking)* technique to maintain the beam centroid stability and address spatial deviation of the incoming light, *Aperture averaging* which use the receiver aperture size to mitigate signal fluctuation, etc...
An interesting technique is the application of an adaptive optics system to correct the incoming beam distorsions. In general, as previously mentioned, an adaptive optics system uses a deformable mirror in order to correct wavefront aberrations, however the electromechanical devices for the steering has the disadvantages to add volume and weight to the receiver, in addition a

deformable mirror is not so easy to implement in an existing system. In order to compensate for these inconveniences we designed a Tip-Tilt adaptive optics system based on the use of a refractive modulator, i.e. a lens; this saves space and allows the system to be implemented on any existing FSO receiver. An important parameter to evaluate the real improvement that the lens can bring to an FSO telecommunications system is the so-called Bit Error Rate (BER). The BER is defined as the rate at which errors occur in a transmission system:

$$BER = \frac{Bits\ errors}{Total\ number\ of\ bits} \tag{2.16}$$

In other terms the bit error rate assesses the full end to end performance of a system including the transmitter, receiver and the medium between the two. If the medium between the transmitter and receiver is good and the signal to noise ratio is high, the BER will be very small. Since in FSO horizontal transmission the medium is the atmosphere, the application of an AO system can enhances the BER performance of the transmission. In particular for small aperture the only tip and tilt effects on the BER is dominant compared to higher order aberration (13) so with the use of our T-T deformable lens we should be able to make an improvement in fiber coupling and consequently, depending on the total bits received, in the bit error rate.

2.4.2 Point-to-point FSO link

In Italy, from an overview of the end of 2020, about 41% of homes are reached by wired optical fiber; it is 18th place for fiber coverage in the EU and 27th in the list of 39 European countries. This figure is not encouraging, especially for areas further away from big cities, whose installation of fiber would require a very high cost for small communities, in cases where the installation itself is possible. This problem may also arise in historical centers or older urban centers where the underground installation of the fiber would risk affecting what is the artistic heritage of the area. In all these cases point-to-point FSO link can be considered as a valid altarnative. In this configuration we found the FSO transmitter located on the top of a building and connected to its LAN (Local Area Network); it transimts the signal trough the free space. On the next building is located the FSO receiver connected, too, to its LAN. Below, in Fig. 2.15, a generic building to building communication system is reported. The performance of point-to-point FSO link is, as said before, strongly dependent on the atmospheric attenuation but, at the same time, atmospheric attenuation is influenced by the weather visibility and link

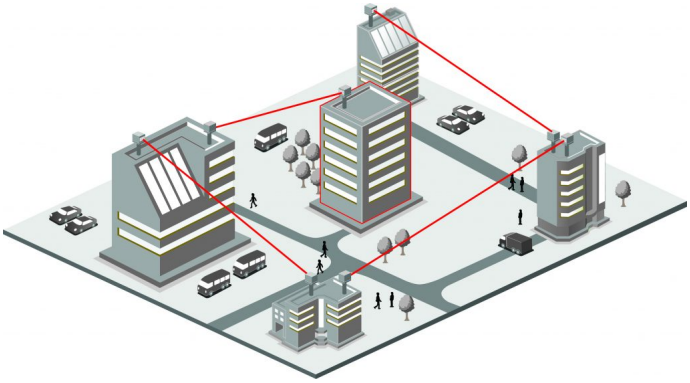

Figure 2.15: Building to building communication system.

distance (21). The equation 2.15 can be written in function of the visibility using the exponential Beers-Lambert Law (23):

$$P_r = P_t e^{(-\sigma Z)} \tag{2.17}$$

where Z is the distance between the transmitter and the receiver [Km] and σ is the *atmospheric attenuation coefficient*

$$\sigma = \frac{3.91}{V}\left(\frac{\lambda}{550}\right)^{-q} \tag{2.18}$$

where λ is expressed in nm and V is the visibility [Km]. The parameter q, according to the *Kim Model*, is the size distribution of the scattering particles:

$$\text{q=}\begin{cases} 1.6 & V > 50Km \\ 1.3 & 6Km < V < 50Km\ (clear) \\ 0.16V{+}0.34 & 1Km < V < 6Km\ (hazy) \\ V{-}0.5 & 0.5Km < V < 1Km\ (foggy) \\ 0 & 0.5V < 0.5Km \end{cases}$$

On (33) several interesting results were found both on the best distance in different weather conditions and on the effect of visibility and attenuation on the signal. It has been found that the wavelength does not affect FSO system performance in clear weather conditions while the maximum link distance varies with variations in weather visibility as well as operating wavelengths. The best performance on maximum link distances at different visibilities is achieved using a wavelength of 1550 nm, as said in 2.4. The performance of point-to-point FSO link is strongly dependent on the atmospheric attenuation; attenuation, in general, decreases with the increase in

visibility and after 0.5 Km with respective visibilities it decreases with the increase in wavelength. The optimum link distance, which will be operated in different weather conditions, is found to be about 400 m. Since events of heavy fog can be considered quite rare, most of the efficiency loss can be attributed to the turbulence present even on days of favorable weather conditions. For this reason our Tip-Tilt correction system can be taken into account to decrease the data loss threshold and to increase the efficiency of fiber coupling in FSO communication systems. To better understand fiber coupling, it is necessary to explain the main characteristics of optical fibers.

2.4.3 Optical fibers

The transmission of light through a fiber is based on the internal reflection of light when it etches between two media with different refractive index at an angle larger than the so called *critical angle*. The propagation of a light rays through a surface between two media with different refractive index, n_1 (core) and n_2 (cladding), follows the *Snell's law*:

$$n_1 sin\theta_1 = n_2 sin\theta_2 \tag{2.19}$$

where θ_1 is the angle of incidence and θ_2 is the refractive angle with respect to the normal of the surface. If $n_2 < n_1$ it is possible to reach the condition of $\theta_2 = \pi/2$ that indicates the *total reflection* of the beam; in this case $\theta_1 = arcsin(n_2/n_1)$ is known as *critical angle*. An optical fiber looks like a very thin cylinder of transparent glass material which acts as a guide to carry light from one end of the fiber to the other. A fiber is composed of four concentrical shells (see Fig. 2.16):

- *The core*: is the innermost area of the fiber where the light beam is confined and travels.
- *The cladding*: is the outer covering of the core made with a dielectric material with a lower refractive index than the core. Its effect is to prevent light leakage from the core as to well as protect it from external contamination.
- *The buffer and the jacket*: are the outermost parts of the fiber which act as a protection from external agents as well as an improvement of the mechanical properties of the fiber. They are made of a polymeric material.

The transmission of light along the fiber is based on its total reflection on the internal surface of the core. Light which is continuously totally reflected

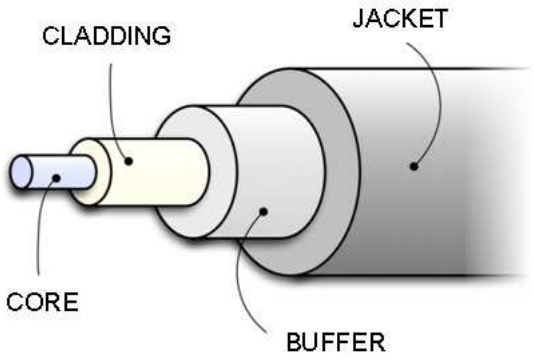

Figure 2.16: Basic structure of an optical fiber.

inside the core will be transmitted till the end of the fiber with minor losses. To reach the total reflection inside the fiber it is necessary that the rays hit the surface between the core and the cladding with an angle greater than the critical one. This means that the rays which are transmitted through the fiber are those which enter the fiber with an angle lower than:

$$\theta_a = arcsin\left(\frac{1}{n_0}\sqrt{n_1^2 - n_2^2}\right) \tag{2.20}$$

where n_0 is the refractive index of the air. If the angle is lower than the acceptance cone the ray will be lost in the outer layers of the fiber. This cone defines a quantity known as *Numeric aperture (NA)*:

$$NA = arcsin\sqrt{n_1^2 - n_2^2} \tag{2.21}$$

Fibers can be classified into two main categories, single-mode fibers and multi-mode fibers, the properties are reported below:

- *Single-mode fibers*: this type of fibers allows the transmission of only one mode, for this reason they are characterized by a very small core diameter (near 4-10 μm). The main advantages are low dispersion, low attenuation, wide bandwidth and longer transmission distance. Disadvantages are relatively few, they are limited to a greater difficulty in centering the spot on the fiber given the small diameter of the core.

- *Multi-mode fibers*: in this case the core diameter is larger than the single-mode case ($\geq$ 20 μm) in order to permit the transmission of multiple modes.

Chapter 3

Tip-Tilt System

In this chapter will be reported the design and characterization of the *Tip-Tilt Lens (TTL)*, completely designed and developed in the CNR-IFN laboratories in Padova. It will be described in parallel with the precedent model in order to highlight the differences and the progresses made. The two lenses differ for different types and number of actuators and for the thickness, all the properties will be reported in the section 3.2. In chronological order we call the first lens *T-T Lens A* and the second one *T-T Lens B*. Before introducing the complete design of the lenses we report the analysis carried out on each single piezoelectric actuator.

3.1 Piezoelectric actuators

Piezoelectric actuators used in this project are Amplified Piezoelectric Actuators (APA), in particular *PICMA Stack Multilayer Piezo Actuators* by *PI*. The model P-883.51 has been used both for *T-T lens A and B*, it is characterized by the properties in Tab. 3.1. A representation of the two sections of PI883.51 is reported below in Fig. 3.1. All the properties can be find in the datasheet (17).

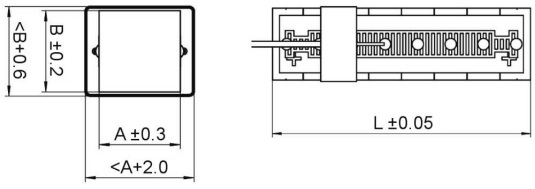

Figure 3.1: Two sections of PI P883.51 where A, B and L are the dimensions of the model reported on Tab. 3.1 (17).

PI P883.51	
Dimensions AxBxL [mm]	3x3x18
Nominal travel range [μ m]	15
Max. travel range [μ m]	18
Blocking force [N]	310
Stiffness [N/μ m]	18
Electrical capacitance [μ F]	0.48
Resonant frequency [kHz]	70

Table 3.1: PI P883.51 main properties.

The stroke amplification on this type of actuators is performed by an elliptical frame around the piezo made of stainless steel completely designed in the CNR-IFN Laboratories in Padova; the magnification is performed along the minor axis while the deformation on the piezo stack occurrs along the major axis (see Fig. 3.2). The difference in terms of actuators of the two lenses is due to the different external frames used. Before assembling the lenses, we aimed our studies on each piezoelectric actuator individually, in particular on the hysteretical behaviour and the resonance frequencies.

3.1.1 Hysteresis

Hysteresis, in general, is the dependence of the state of a system on its history. In the case of piezoelectric ceramics it means that the displacement associated to a particular voltage is not the same every time; in other words the corresponding displacement curves in the voltage lift and return intervals do not overlap. The hysteresis curve of the single piezoelectric actuator has been retrieved taking one image every 10V from 0V to 100V starting from an offset of 50V. These images were obtained using the *Dynamic optic*'s proprietary software *Photonloop* for the control of the actuators, a microscope with 10x zoom and an IDS UI-3060 scientific camera, as reported in Fig. 3.2; all the images have been analyzed with the software *ImageJ*. During this analysis it has been obtained also the maximum stroke of the actuators, important to compare, later, the theoretical maximum angular displacement of the lens with the real one. The displacement-voltage diagrams for the piezeoelectric actuators of the *T-T lens B* are reported below in Fig 3.3 considering an associated error resulting from the propagation of an uncertainty of 3 px

per axes; not to be repetitive the results of the *T-T lens A* can be found in appendix A in Fig. A.1.

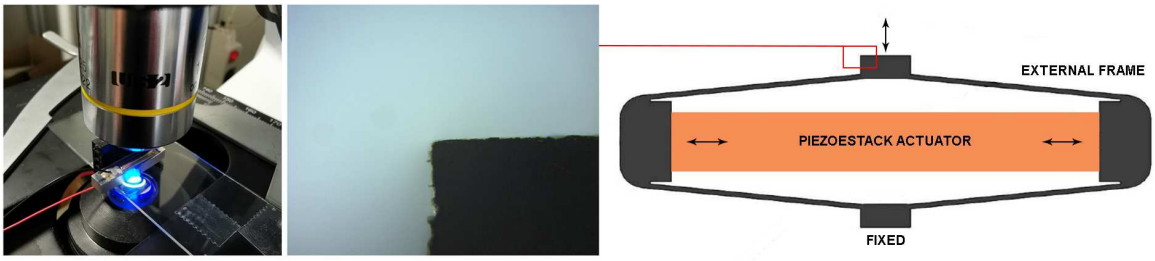

Figure 3.2: On the left side image the setup is shown while on the right side the amplified piezoelectric actuator's sketch is reported where has been highlighted the corner used for the measurement.

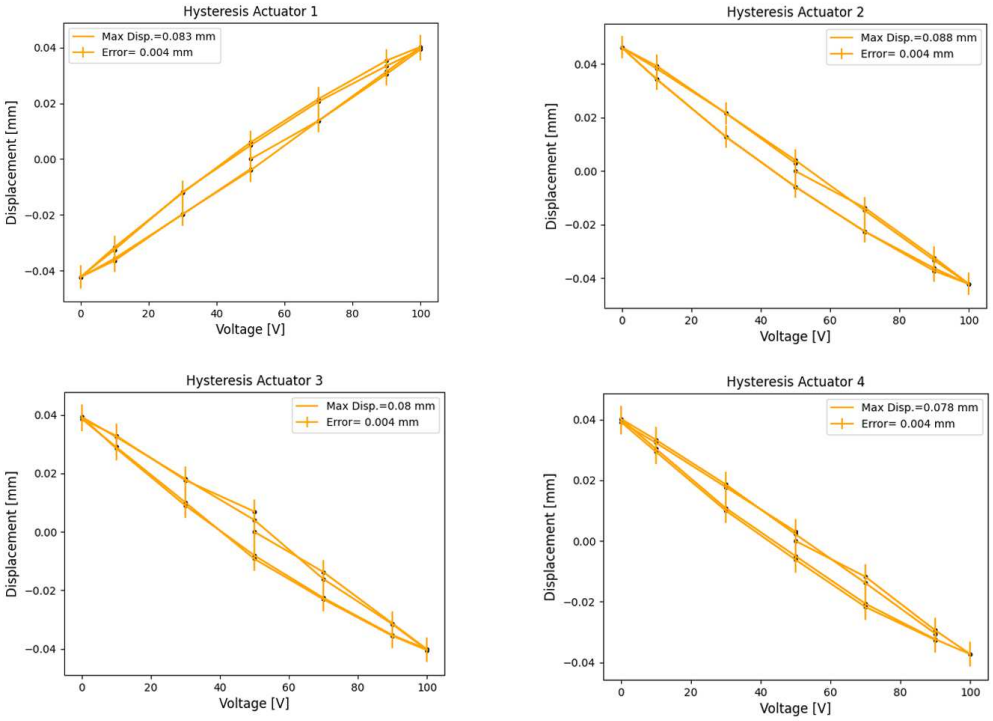

Figure 3.3: Hysteresis cycle of the four piezoelectric actuators used in the *T-T lebs B* where it is highlighted the maximum displacement.

In our system the presence of hysteresis is not a problem since we can operate with a closed loop feedback.

3.1.2 Resonance frequencies

Other important properties that have to be taken into account are the *resonance frequencies* of the piezoelectric actuators. The oscillation of the piezo stack during its operation can be near a natural frequency of the actuator and lead to a the vibration of the elliptical external frame with a consequent worsening of the performances. Our aim is to verify that the natural frequencies of the actuators are higher than the typical frequencies at which the actuators works. Firstly, the resonance frequencies were theoretically studied in design phase with the software *Comsol* considering one of the two bases of the actuator constrained as in the real case where the actuator is part of the lens; On Tab. 3.2 six theoretical resonance frequencies are proposed with an example image reported in Fig. 3.4.

Resonance Frenquencies [Hz]			
f_1	938.08	f_4	5368.6
f_2	1228.5	f_5	5797.1
f_3	1292.5	f_6	10870

Table 3.2

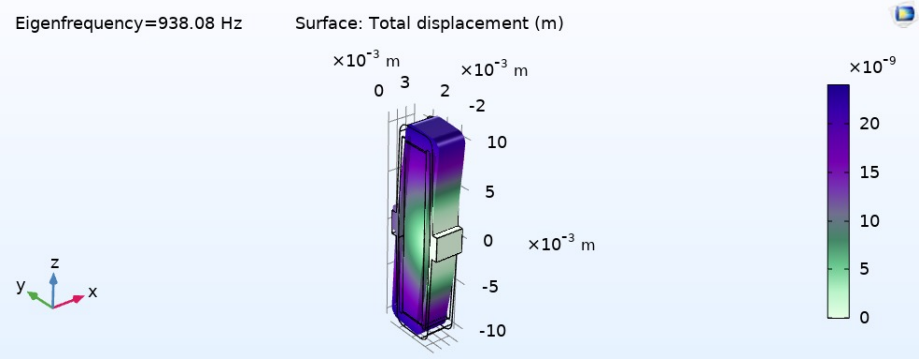

Figure 3.4: Comsol design of the external frame with the first resonance frequency.

In order to retrieve the real resonance frequencies of each single piezoelectric actuator a setup has been created with these components:

- *Microscope*: used with a 10x zoom to obtained images of the actuator's displacement; it is shown in Fig. 3.2 and it is the same used for hysteresis analysis.

- *Function generator*: used to create a sinusoidal signal with a variable frequency and fixed peak-to-peak amplitude of 1 V and a starting point offset of 1 V.
- *Amplifier*: since the range accepted by the actuators goes from 0 to 100 V we used an amplifier with gain factor 50 obtaining a peak to peak amplitude equal to 50 V centered on 50 V.
- *Oscilloscope*: used as a verification instrument.

With this setup, we have given as input the sinusoidal signal created with the generator, gradually increasing the frequency from 100 to 1100 Hz. We have, thus, sampled with the microscope the amplitude of the external frame oscillation of for the number of frequencies. What we obtained is a frequency-displacement graph, shown in Fig. 3.5 with an example of the 900 Hz image.

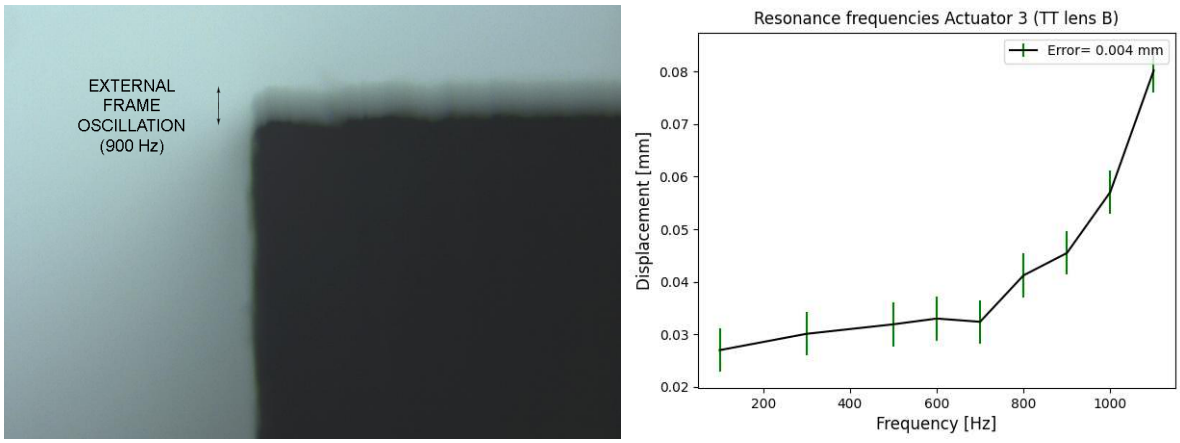

Figure 3.5: On the left side an example image relate to the frequency of 900 Hz is reported with the relative oscillation amplitude of the external frame. On the right side can be found the displacement-frequency graph.

As we can see the actuators used in the *T-T lens B* are characterized by resonance frequencies that increase with increasing frequency and start to become important beyond about 900 Hz confirming our *Comsol* analysis. We performed the same test on the piezoelectric actuators used on *T-T lens A*, the results obtained are shown in Fig. 3.6. In the case of *T-T lens A* the two piezolectric actuators are characterized by multiple resonance peaks on almost the entire frequency spectrum making the lens A unstable. Considering that the working frequency of the lens is mostly below 900 Hz the lens

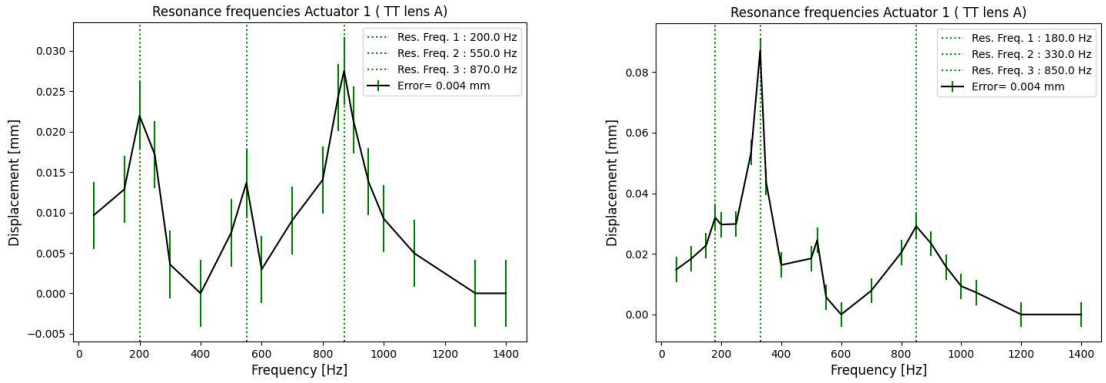

Figure 3.6: Resonance frequencies of piezoelectric actuators 1 and 2 used in *T-T lens A*.

B is clearly superior to its counterpart because it has negligible resonance frequencies on the working frequency range. In the next section the design and the complete analysis of the *Tip Tilt lenses* are reported.

3.2 Lens Design

The two lenses have been designed using the same concept; starting from the first surface, we used:

- *T-T lens A*: A square plane glass 25x25x1 mm. This surface is supported by two piezoelectric actuators and a fixed pivot located on three vertex of the slide.
  T-T lens B: A square plane glass 25x25x1 mm supported by four piezoelectric actuators situated on the four vertex. A design of the lens B is reported below in Fig. 3.7 while the design of lens A is reported in appendix A.

- A cylinder of Sylgard gel. *Sylgard* is a transparent silicon elastomer with good dielectric properties. We chose *DOWSIL™ Q3-6575* produced by *DOW* with a refractive index $n \approx 1.43$. All its properties can be found in (10).

- A second plane square glass rotated by 45°.

The principle used is very simple, the light beam arrives meeting the deformable face of the lens, which through the use of piezolectric actuators

can change its inclination thus deflecting the outgoing beam. We decided to use the mobile face as first surface to achieve a greater leverage on the detector. The properties of the two models are proposed on Tab. 3.3.

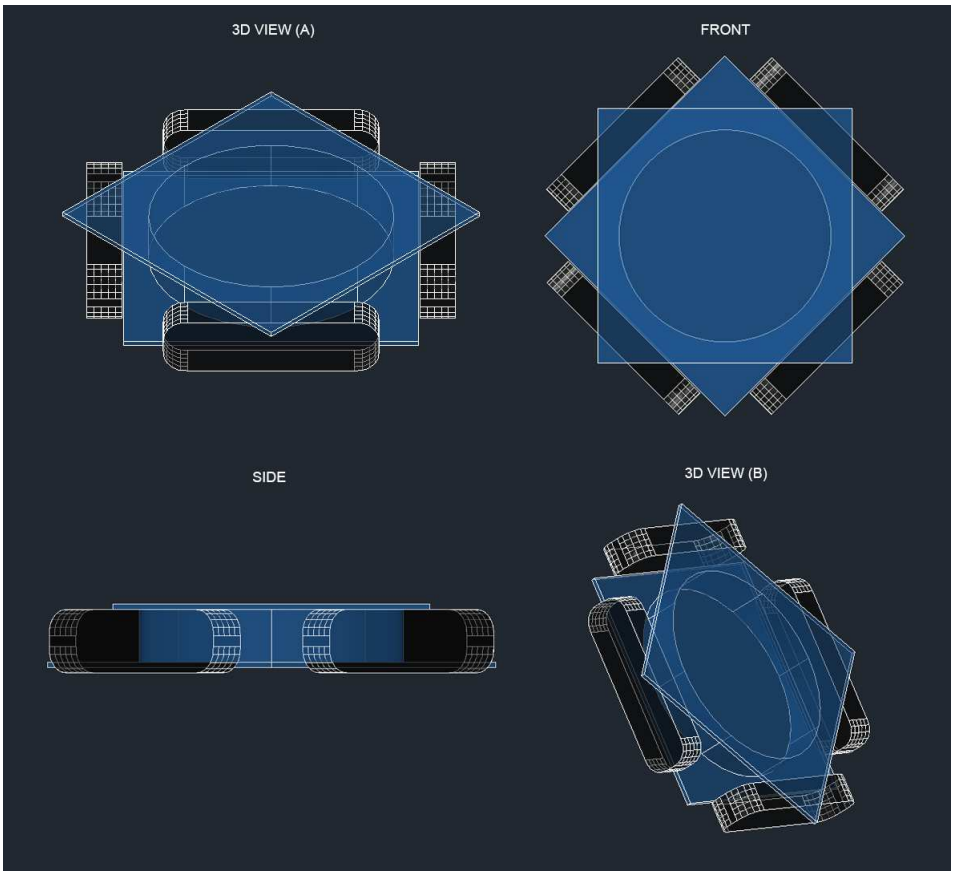

Figure 3.7: Design of the *T-T lens B* in four different views. The blue parts indicate the refractive parts of the lens while the black rectangles simulates the four piezoelectric actuators which are connected to the fixed structure.

In the next sections the following studies carried out on the lenses will be reported:

- **Studies on the maximum angular capacity**
- **Analysis of the chromatic aberration effects**
- **Rejection band**
- **Experiment in laboratory with a source of aberration**

	Lens A	Lens B
Number of actuators	2	4
Diameter [mm]	≈ 25	≈ 23
Thickness [mm]	15	5
Maximum actuators strokes [mm]	± 0.063 (± 0.004)	± 0.041, ± 0.044 (± 0.004)
	± 0.106 (± 0.004)	± 0.040, ± 0.039 (± 0.004)
Measured resonance frequencies [Hz]	P1: $\approx$ 200, 550, 870	P1, P2, P3, P4: $> \approx 900$
	P1: $\approx$ 330, 520, 850	

Table 3.3: Properties of the two lenses where P indicates the piezoelectric actuator.

3.3 Angular displacement

After the characterization of each piezolectric actuator we calculated a certain angular displacement of the lens from the maximum excursion of the actuators itself but during our analysis we found a slight difference between the angular displacement of the spot on the detector compared to the expected one. The comparison is shown below.

3.3.1 T-T Lens B

T-T Lens B has 4 piezoelectric actuators (P1, P2, P3, P4) with maximum stroke as detailed below:

- $S_{P1} = \pm 0.041 \pm 0.004$ mm
- $S_{P2} = \pm 0.044 \pm 0.004$ mm
- $S_{P3} = \pm 0.040 \pm 0.004$ mm
- $S_{P4} = \pm 0.039 \pm 0.004$ mm

each experimentally measured.
To improve the displacement of the lens we coupled the piezoelectric actuators two by two reaching maximum strokes as follows:

- P1 & P4 $\rightarrow S_{1,4} = \pm S_{P1} \pm S_{P4} \approx \pm 0.080 \pm 0.008$ mm

- P2 & P3 $\rightarrow S_{2,3} = \pm S_{P2} \pm S_{P3} \approx \pm 0.088 \pm 0.008$ mm

We report below the theoretical displacement of the spot on the detector Δx_1 taking into account the maximum stroke $S_{1,4} = S$ and the following properties, see Fig. 3.8:

- L = 25 mm
- f= 230 mm
- $n_{air} \approx 1$
- $n_{syl} \approx 1.43$

$$\alpha = \frac{S}{L} = \frac{0.08}{25} \approx \pm 3.2\ mrad \tag{3.1}$$

$$\beta = \frac{n_{air}}{n_{syl}}\alpha = \frac{1}{1.43}3.2 \approx \pm 2.24\ mrad \tag{3.2}$$

$$\gamma = \alpha - \beta = 3.2 - 2.24 \approx \pm 0.96\ mrad \tag{3.3}$$

$$\delta = \frac{n_{syl}}{n_{air}}\gamma = \frac{1.43}{1}0.96 \approx \pm 1.37\ mrad \tag{3.4}$$

$$\Delta x_1 = \delta \cdot f = 0.00137 \cdot 230 \approx \pm 0.32\ mm \tag{3.5}$$

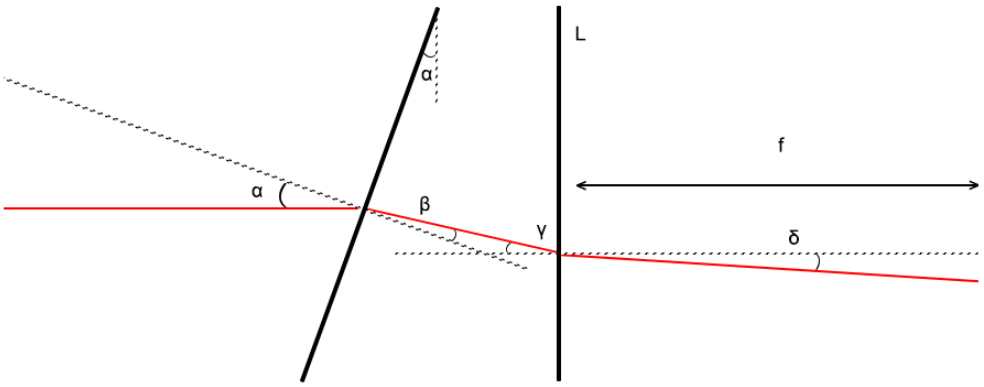

Figure 3.8: Design of the system

the calculation for the other couple of piezoelectric actuators is similar. From the theoretical analysis of the angular displacement we expect ±0.32 mm on

the detector but experimentally we don't observe it. To retrieve the real shift of the spot we set three different voltages on the actuators obtaining the real position in pixel of the beam. Three images are obtained, one for 50 V (zero position), one for 0 V and one for 100 V as reported below:

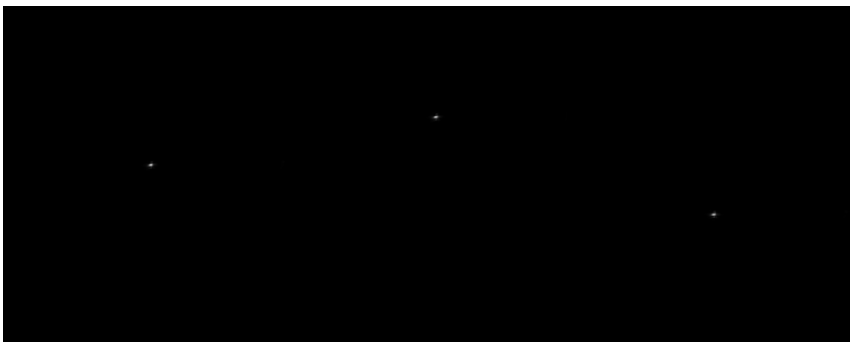

Figure 3.9: Images of the spot displacement for lens B. From the left side there is the 50 V, 100 V and 0 V position.

From the difference of the centroids pixel positions and considering a pixel size of 5.86 μm we obtained a displacement of:

- $\Delta x_2(0 - 50V) = 0.23$ mm
- $\Delta x_2(50 - 100V) = 0.20$ mm

We can, now, retrieve the real angular displacement of the lens in order to compare it with the theoretical one using $\Delta x_2(50 - 100V)$.

$$\delta_2 = \frac{\Delta x_2}{d} = \frac{0.20}{230} = \pm 0.87\ mrad \tag{3.6}$$

$$\gamma_2 = \frac{n_{air}}{n_{syl}}\delta_2 = \frac{1}{1.43}0.87 \approx \pm 0.61\ mrad \tag{3.7}$$

$$\alpha_2 = \frac{\gamma_2}{1 - \frac{n_{air}}{n_{syl}}} \approx \pm 2.03\ mrad \tag{3.8}$$

It is evident that the real angular displacement is smaller than the theoretical one, in particular:

$$\alpha - \alpha_2 \approx 1.17\ mrad \tag{3.9}$$

that is translated in a difference on the maximum strokes of the piezoelectric actuators of:

$$S - S_2 \approx S - L \cdot \alpha_2 \approx 0.08 - 25 \cdot 0.00203 \approx 0.08 - 0.051 \approx 0.029\ mm \quad (3.10)$$

It results in a difference of ≈ 36% with respect to the maximum stroke obtained in the previous section during the hysteresis analysis. This difference can be due to an elastic resistance of the thin Sylgard gel.

3.3.2 T-T Lens A

In this case *T-T lens A* has a pivot and two piezoelectric actuators (P1, P2) with maximum stroke as detailed below:

- $S_{P1} = \pm 0.063 \pm 0.004$ mm
- $S_{P2} = \pm 0.106 \pm 0.004$ mm

this difference in the first two actuators is due to their manual manufacture. Using the same procedure adopted with the lens B, we retrieve the theoretical displacement of the spot on the detector Δx_1 taking into account the maximum strokes S_{P1}, S_{P2} and a focal length of 300 mm:

- L = 25 mm
- f= 300 mm
- $n_{air} \approx 1$
- $n_{syl} \approx 1.43$

As before we obtained two theoretical displacements $\Delta x_{1,p1} = \pm 0.325$ mm for S_{P1} and $\Delta x_{1,p2} = \pm 0.547$ mm for S_{P2}. From the difference of the centroids pixel positions and considering a pixel size of 5.86 μm we obtained $\Delta x_{2,p1} = \pm 0.12$ mm for S_{P1} and $\Delta x_{2,p2} = \pm 0.21$ mm for S_{P2}.

Now, doing the reverse procedure, we can retrieve the real angular displacement of the lens and consequently the strokes of the actuators, as done with the *TT lens B*; $\alpha_{2,p1} = 0.93$ mrad and $\alpha_{2,p2} = 1.633$ mrad were obtained. As in the previous case, the real angular displacement is smaller than the theoretical one:

$$\alpha_{p1} - \alpha_{2,p1} \approx 2.9 - 0.93 \approx 1.59\ mrad \quad (3.11)$$

$$\alpha_{p2} - \alpha_{2,p2} \approx 4.9 - 1.63 \approx 2.61\ mrad \quad (3.12)$$

Figure 3.10: Images of the spot displacement for lens A. From the left side there is the 100V and the 0 V position for P1 and 100V and 0V position for P2.

The difference on the maximum strokes of the 2 piezoelectric actuators are:

$$S_{p1} - S_{2,p1} \approx S_{p1} - L \cdot \alpha_{2,p1} \approx 0.063 - 25 \cdot 0.00093 = 0.063 - 0.023 \approx 0.040\ mm \tag{3.13}$$

$$S_{p1} - S_{2,p2} \approx S_{p2} - L \cdot \alpha_{2,p1} \approx 0.106 - 25 \cdot 0.00163 = 0.106 - 0.041 \approx 0.065\ mm \tag{3.14}$$

In this case, for the lens A, there is a more important difference of $> 50\%$ with respect to the maximum strokes of each piezoelectric actuator. This effect can be due to the different external frame of the piezoelectric actuators used with respect to the *T-T lens B*, it has been projected with a thinner structure so the Sylgard resistance has more important resistance effects.

3.4 Chromatic aberration

In Chapter 2 we introduced what are the advantages of using an adaptive refractive element compared to a mirror, but the lens brings with it a problem not a priori negligible , that is the chromatic aberration. Considering transparent media, such as glass, the refractive index decreases as the wavelength increases:

$$\frac{dn}{d\lambda} < 0 \tag{3.15}$$

this implies that shorter wavelength rays will be deflected more than longer wavelength rays. This mechanism is the basis of chromatic aberration. In our case, the lens can be part of different type of correcting system, in the case of FSO communication this problem is not taken into account because it is used a single wavelength but for an astronomy application this effect has to be considered. The lens behaves as a prism so there is two main effect on the beam; a variation on the focal length and an angular deviation in function of the wavelength. To analyze the impact of this aberration on the system we

performed a simulation using the ray tracing sofwtare *Zemax OpticStudio*. The setup, reported in Fig. 3.11, is:

- Collimated beam with 20 mm diameter composed by wavelengths: 0.7 μm and 0.46 μm.
- Hyperbolic mirror with 25 mm of diameter for beam focusing.
- *T-T lens B* with the second surface tilted by the maximum angular displacement of 3.2 mrad. In first approximation it has been used a lens with the refractive index of the Sylgard gel without taking into account the presence of the two thin external glass layer. This can be done because the effect of the Sylgard layer is to be considered more important; it represents the most of the lens thickness.

The collimated source is reflected and focalized by the hyperbolic mirror, choosed instead of a converging lens in order to avoid an additional source of chromatic aberration. We highlighted the two wavelengths by assigning a green color to 0.46 μm and blue to 0.7 μm.

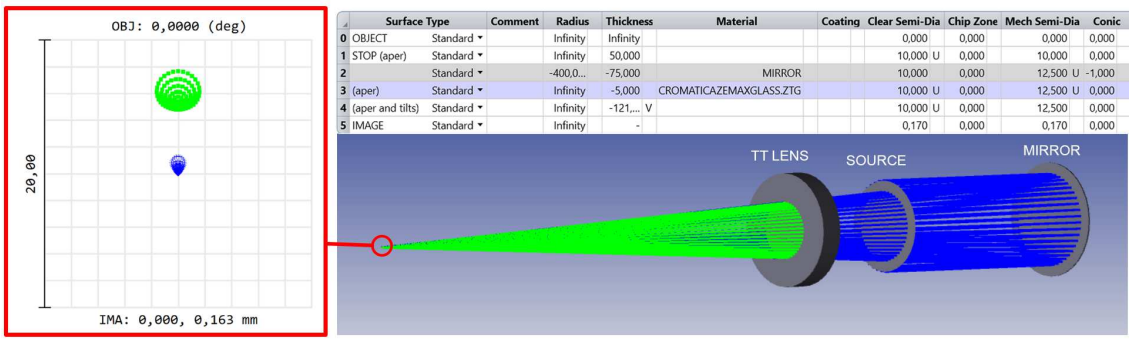

Figure 3.11: Simulation of chromatic aberration introduced by *T-T lens B*. On the right side lens data frame and 3D reconstruction are reported. On the left side it is shown the spot diagram on the screen.

From the spot diagram we recovered a distance from the two spots of $\Delta y \approx 4.8\ \mu m$ that, assuming a distance from the lens d, it translates into an angular displacement of:

$$\theta \approx \frac{\Delta y}{d} = \frac{4.8}{126500} = 3.79 \cdot 10^{-5} rad \tag{3.16}$$

Now, if we consider a system limited only by diffraction, we obtain two spots with an angular diameter:

$$\theta_{700nm} = 2 \cdot \frac{1.22\lambda}{D} = 2 \cdot \frac{1.220.7}{20000} = 8.54 \cdot 10^{-5} rad \tag{3.17}$$

$$\theta_{460nm} = 2 \cdot \frac{1.22\lambda}{D} = 2 \cdot \frac{1.220.46}{20000} = 5.61 \cdot 10^{-5} rad \tag{3.18}$$

much greater than the distance between the two centroids. This implies that the chromatic aberration is slightly present with this type of lens. This effect can be mitigated in astronomy using a filter centered on the desired wavelength.

3.5 Rejection Band

The temporal statistic of aberration is an important parameter to take into account because it defines how fast and efficient the correction system should be. In our case, to have an idea on the T-T lens performances, we studied what is called *Rejection band*. The rejection bandwidth is defined as the frequencies that are lost or removed from a source signal. In our system the rejection band represents the frequencies that the lens is not able to sustain and correct and, instead to compensate the distortions, it tends to amplify it. The procedure to retrieve the rejection band was to provide a stimulus to the lens and see how well it was reproduced. As input we generated a sinusoidal function vis software in the form of zernike modes whose amplitudes along the two axes have been limited to stay within the working range. From the difference between the input commands and what the lens is really able to emulate we have been able to derive the rejection frequencies. Once the function was generated we ran tests of 30 seconds each by varying the frequency from 1 to 5 Hz and then from 5 to 50 Hz in steps of 5. This analysis was conducted by varying the gain of the control system k from 0.1 to 0.25 in steps of 0.05 for the lens A and from 0.1 to 0.5 in steps of 0.1 for lens B. The entire procedure has been managed by the software *Photonloop* with parameters reported in Tab. 3.4. Analytically we have to retrieve the residual amplitude resulting from the input and the output, we proceeded as follow: From the software *Photonloop* we registered the input Zernike modes and the output that is the real Zernike modes that the lens are performing. Once that we had the two signals we performed the difference between the amplitude of the input signal A_{input} and the amplitude of the output signal A_{output} in both the x and y axis. If the lens efficiently

reproduces the modes, the two signals are in phase so the residual amplitude A_{res} is very low. When the frequency starts to rise the lens are no more able to follow perfectly the input commands so the residual amplitude start to rise itself. The residual amplitude is defined as:

$$A_{res} = \frac{\sqrt{A_{res,x}^2 + A_{res,y}^2}}{\sqrt{A_{input,x}^2 + A_{input,y}^2}} \tag{3.19}$$

The results for the lens A and lens B are reported in Fig. 3.12 and Fig. 3.13. From the graphs it is evident that with the lens B we reached an higher level of performance; the cutting frequency for the lens B is near 16 Hz with k=0.4 against 10 Hz of the lens A reached with k=0.15. The cutting frequency is the frequency at which the curve intercept the 0 value. Thanks to the evolution of the external frame of the piezoelectric actuators and to the new lens configuration we have been able to achieve more than 50% with respect to the lens A.

Photonloop parameters	
Framerate [Hz]	$\approx$ 1000
Pixel clock [Hz]	$\approx$ 470
Exposure [ms]	$\approx$ 0.02

Table 3.4

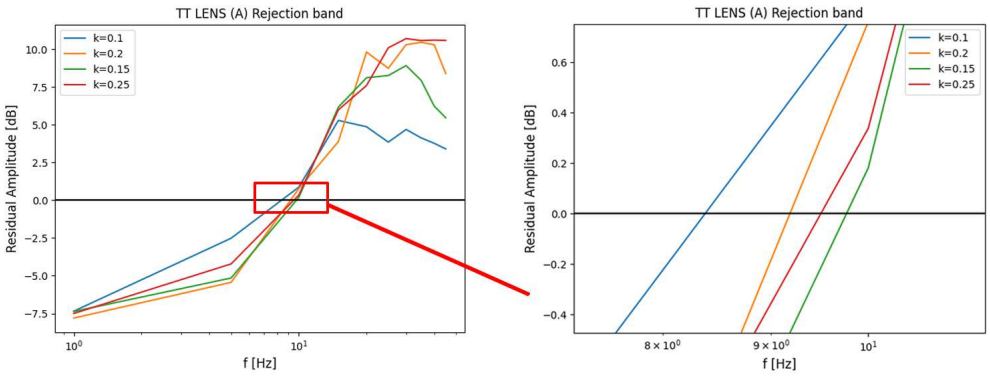

Figure 3.12: Rejection band of the *T-T lens A* where the results for each gain k are reported.

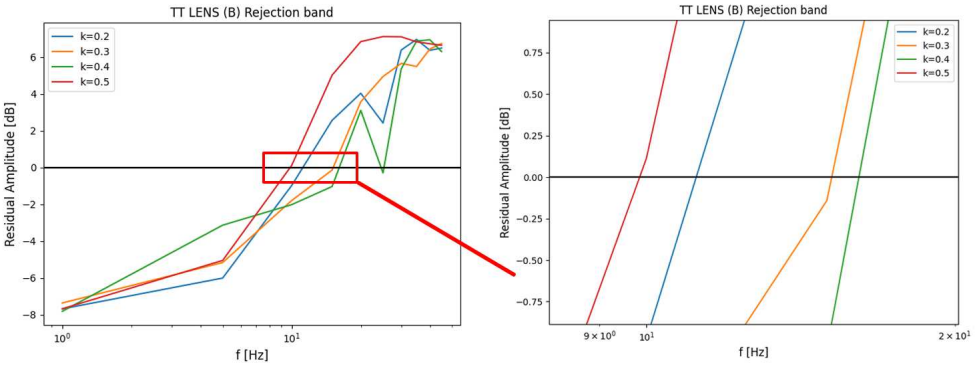

Figure 3.13: Rejection band of the *T-T lens B* where the results for each gain k are reported.

3.6 Correction of closed loop generated aberration

We tested the *T-T lens B* in the laboratory with an experiment that simulates a real outdoor correction situation. The aberration, in our indoor experiment, has been simulated using a *Multi-actuator Adaptive Lens (MAL)* (3) mentioned in Chapter 2 that can reach up to the 4th order of the Zernike polynomials. The setup is reported below in Fig. 3.14.

3.6.1 Experimental setup

For the experiment we built the following setup on the optical bench:

- 808 nm collimated laser beam
- Multi-actuator Adaptive Lens for generating aberrations
- Beam splitter to split the beam
- Shack-Hartmann WFS for the MAL control
- *T-T lens B* for correcting aberrations
- Camera for the analysis and for the T-T lens control

The beam was focalized into the camera and recollimated after the beamsplitter to enter on the S-H WFS. The aberration has been generated starting from a real aberration measured in a precedent experiment with a 30 cm telescope; it has been resized on a 5 cm aperture in order to be as faithful as

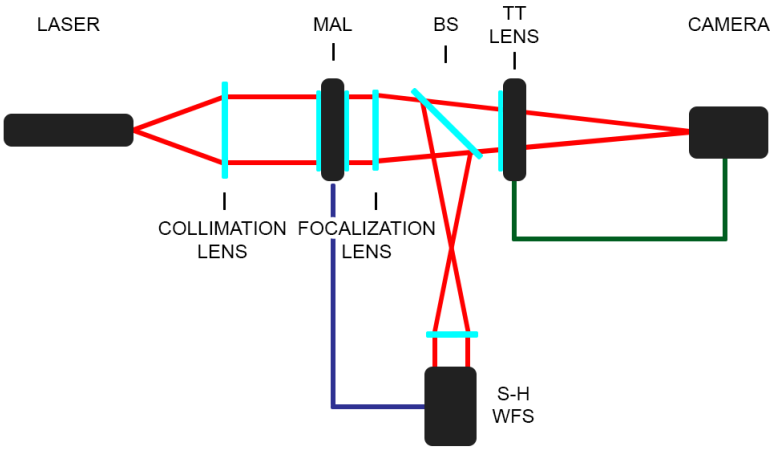

Figure 3.14: System configuration where the two control loop for the adaptive lenses are highlighted, in purple the MAL control end in green the T-T lens control.

possible to an outdoor experiment. This aperture has been chosen because it is the one we intend to work with. The frequency of the turbulence has been set to 500 Hz. The two control system has been managed with the software *Photonloop* where the correcting frequency has been maintained close to 1.1 Khz. The results are reported in the next paragraph.

3.6.2 Tip-Tilt correction

To retrieve the correction performances of the lens we generated two graphs, one for Tilt in X direction and one for Tilt in Y direction, where the difference between the uncorrected beam and the closed loop corrected beam are reported. The graphs were constructed obtaining the distance (*slopes*) between the centroids and the central reference point, from the software *Photonloop* as functions of time. The two plots are proposed below in Fig. 3.15. It is clear that the presence of the T-T lens brings a real improvement, we passed from a standard deviation $\sigma_{nocorr} = 82.2\ \mu rad$ to a $\sigma_{corr} = 30\ \mu rad$ for Tilt along X, that is more than 60%. The same improvements were achieved in the other direction, even there we corrected about 60% of the total deviation.

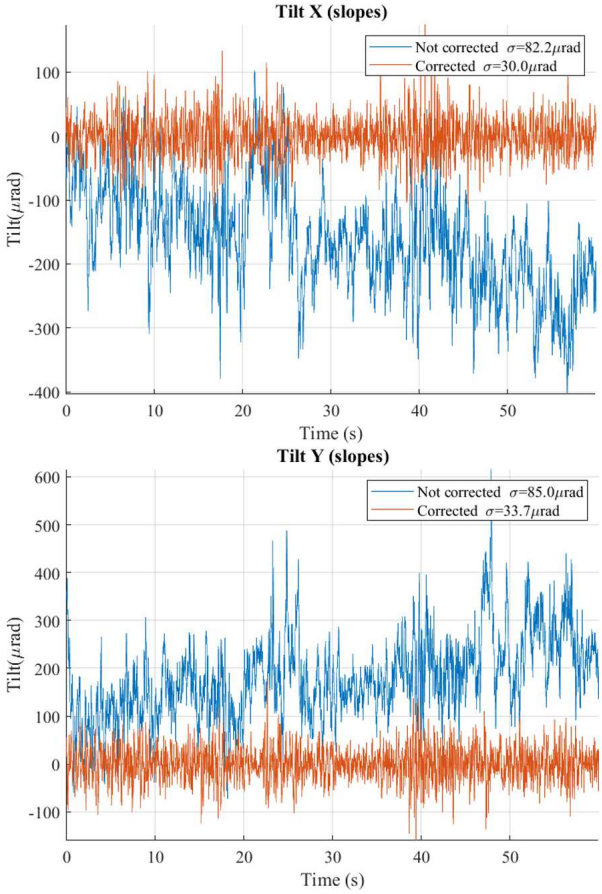

Figure 3.15: Tilt in X and Y directions where the blue line is the case with no correction and the orange one is the closed loop correction case.

3.6.3 Power Spectral Density (PSD) and Rejection band

Understanding how the strength of a signal is distributed in the frequency domain is important for our purpose. The Power Spectral Density (PSD) (7) represents the proportion of the total signal power contributed by each frequency component of a voltage signal. In our case, for the PSD computation, has been used the *Pwelch method* (34) on the Zernike modes for the two axis. From the ratio between the two power spectral densities has been obtained the *Rejection band* as follow:

$$RB = 20\log_{10}\left(\frac{PSD_{corrected}}{PSD_{uncorrected}}\right) \tag{3.20}$$

whose result is shown below in Fig. 3.16. The analysis has led to a cutting frequency of about 4.4 Hz, smaller than the cutting frequency obtained on

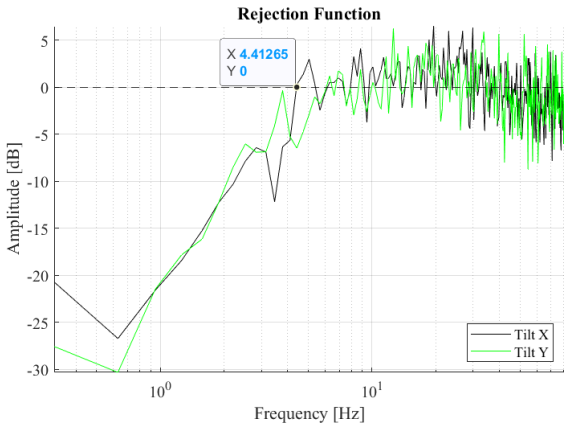

Figure 3.16: Rejection band where the blue line is the X axis and the orange one is the Y axis.

the section 3.5 with the sinusoidal input function. This is due to a quite different type of signals, in the previous case we had a single frequency signal with a fixed amplitude instead of a multiple frequency signal with different amplitudes as in this case. So when the lens has to deal with a very disturbed signal the performance drops, as expected.

3.6.4 Centroids

To consolidate the results obtained during this experiment, we considered the distribution of the centroids on the camera. This tells us how well the T-T lens is able to keep the beam within a certain area around the centre. These results are important on the improvement on the fiber coupling efficiency in FSO communications that will be proposed on the next chapter. We produced a scatter plot which shows the position of the centroid for each acquisition and an histogram with the density of the centroids projected on the X axis. The graphs are proposed below (Fig. 3.17). From the graphs of the centroid position along the X axis, it is possible to notice that we are able to reach about a 63% of tip tilt correction. This percentage can be found also comparing the two deviations on the mean distance diagram. So from the experiment conducted in the laboratory to simulate a possible external situation we obtained encouraging results. The T-T lens is able to correct tip-tilt aberration by about 60% with a cutoff frequency derived from the rejection analysis of about 4.4 Hz.

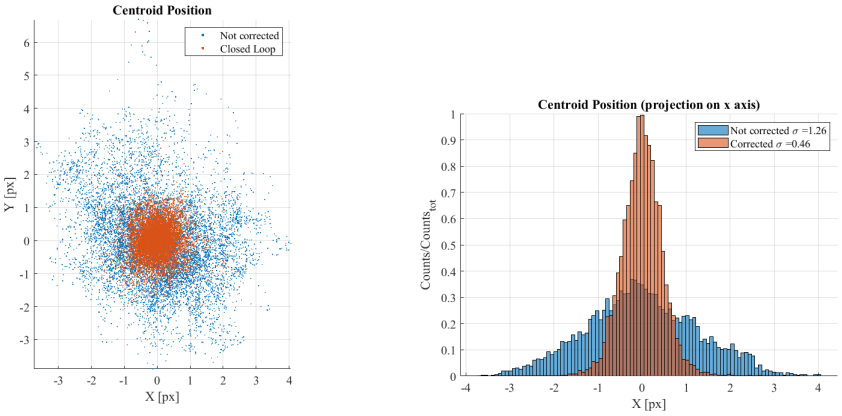

Figure 3.17: Centroids analysis where the blue color is associated to the uncorrected case while the orange one is associated to the case with closed loop correction.

Chapter 4

Improvement of the fiber coupling efficiency after horizontal optical transmission

Fiber coupling at the receiver is of fundamental importance to increase FSO communication efficiency and diminish the Bit Error Rate (BER). A 20 m free space transmission of a collimated laser diode was performed between two telescope mounts. The beam has been focused and injected into a multi-mode optical fiber, tip and tilt were corrected using T-T lens B in closed loop.

4.1 Experimental setup

The experiment was conducted by simulating an FSO transmission using a transmitter and a receiver separated by a distance of 20 m, the complete setup design is reported in Fig. 4.1 and Fig. 4.2. The transmitter is mounted in a *Celestron CGX* equatorial mount and uses a collimated IR multi-mode diode laser with $\lambda = 850$ nm. The elements composing the receiver are all mounted on a rectangular plate fixed to an altazimuth mount. The beam is focused by the lens L1 (see Fig. 4.1) and passes through a beamsplitter. The reflected beam is focused on the optical fiber mounted on a Thorlabs Z825B motorized stage which permits a translation along the optical axis. Manual adjustment of the position on the perpendicular plane is also possible. Since we are using a multi-mode diode laser as source we opted for a multi-mode Thorlabs fiber instead of a single-mode one. At the end of the fiber a Thorlabs PSD PDA36A-EC is positioned. The transmitted beam has been focused on a scientific *IDS* camera for the control of the *T-T lens B* located between

the lens L1 and the beamsplitter.
If we consider our diode laser with $\lambda = 850$ nm, the beam aperture at the receiving d $\approx$ 25.4 mm and the focal length F of the lens L1, with the diffraction limited equation we obtained the spot diameter D_{beam} and the spot numerical aperture NA_{beam} on the detector:

$$D_{beam} = 2.44\frac{\lambda}{d}F = 2.44\frac{850 \cdot 10^{-6}}{25.4}300 = 24.5\ \mu m \tag{4.1}$$

$$NA_{beam} = 2 \cdot arctan\left(\frac{d}{F}\right) = 2 \cdot arctan\left(\frac{12.7}{300}\right) \approx 0.09\ rad \tag{4.2}$$

we used a single-mode fiber with a core diameter of 25 μm and a numerical aperture of 0.1 rad which matches the numerical aperture of the setup.
As we can see in Fig. 4.2 and Fig. 4.1 a tracking system has been implemented for a coarse alignment of the mounts. The tracking system is composed by a collimated diode laser ($\lambda = 850$ nm) on the receiver mount and a IDS scientific camera (mod. UI-3060CP) with a focusing lens on the transmitter mount.

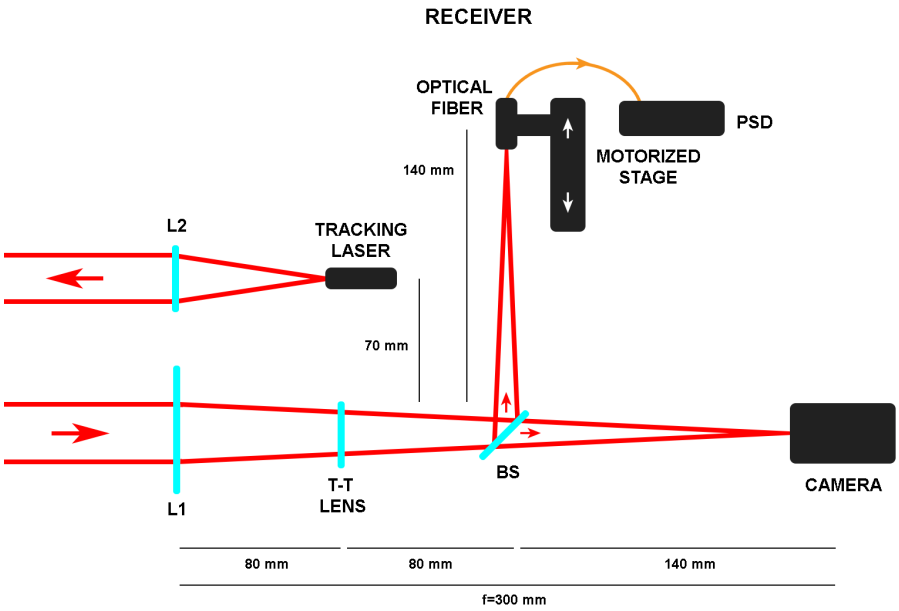

Figure 4.1: Receiver setup of the FSO transmission system. The laser directed to the right comes from the transmitter and passes through the elements that make up the receiver. The laser directed to the left is the source of the tracking system.

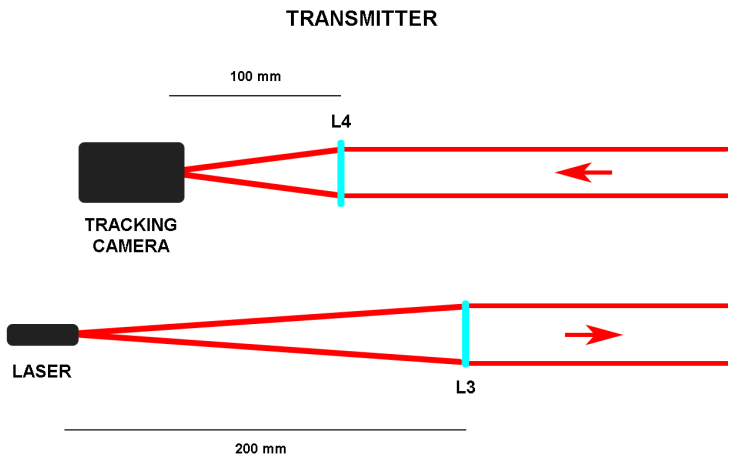

Figure 4.2: Transmitter setup of the FSO transmission system. The laser directed to the right forms the source of our transmission while the laser directed to the left enters into the camera of the tracking system.

4.1.1 Tracking system

In our experiment both the transmitter and the receiver are mounted on two astronomical mounts. This can causes misalignments due to the presence of the wind or possible vibrations and oscillations of the ground. We developed a tracking system capable of keeping the mounts aligned throughout the duration of the experiment with a *Proportional–Integral–Derivative (PID)* control. The basic idea has been to calculate the centroid position on the IDS camera using the momenta of the image with the openCV library (library of programming functions mainly aimed at real-time computer vision) and, on the basis of the difference between the actual position and the desired one, to retrieve the output commands for the motorized mount from the reconstruction matrix as explained in Chapter 2.3. The proportional component depends only on the difference between the set point and the centroid positions; the proportional gain (K_c) determines the ratio of the output response to the error term. The integral component sums the error terms over time; therefore, it continually increases over time unless the error is zero. Its effect is to minimize the difference between the actual position and the target one. The derivative component is inversely proportional to the process variable. Both the tracking software and the UI has ben written in *Python* using also *Celestron CPWI* and *Ascom* software to interface with the CGX mount.

All the components of the transmission system are reported below:

Transmitter:

- **Laser**: $\lambda = 850$ nm Diode Laser
- **Lens 3 (L3)**: f = 200 mm, D = 1 inch
- **Tracking camera**: *IDS* mod. UI-3060CP
- **Lens 4 (L4)**: f= 100 mm, D = 1 inch

. **Receiver**:

- **Lens 1 (L1)**: f = 300 mm, D = 2 inch
- **T-T lens B**
- **Beamsplitter**: cubic beamsplitter 70:30
- **Camera**: *IDS* mod. UI-3060CP
- **Optical fiber**: multi-mode fiber 400-500/700-1400 nm Thorlabs mod. M67L01, $D_{core} = 25\ \mu m$, NA = 0.1 rad
- **Motorized stage**: Thorlabs Z825B with Thorlabs brushed motor controller KDC101
- **Detector**: PSD Thorlabs PDA36A-EC
- **ADC Device (Analogic to Digital Converter)**: National Instrument USB-6001
- **Tracking laser**: $\lambda = 850$ nm
- **Lens 2 (L2):** f = 50 mm, D = 1 inch

4.2 Methods

The transmitter and the receiver have been placed at a 20 m distance from each other. The transmitter was placed outside the laboratory while the receiver was inside. The beam passed through a window where the air vortexes cause more turbulence compared to the rest of the beam path (see Fig. 4.3 and Fig. 4.4). The test has been conducted the March 8^{th}, 2022; the weather was sunny and slightly windy.

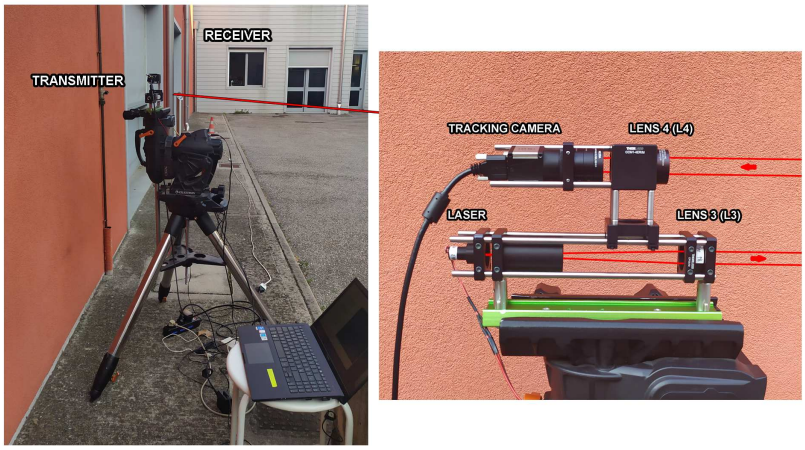

Figure 4.3: Transmitter setup of the FSO comunication system.

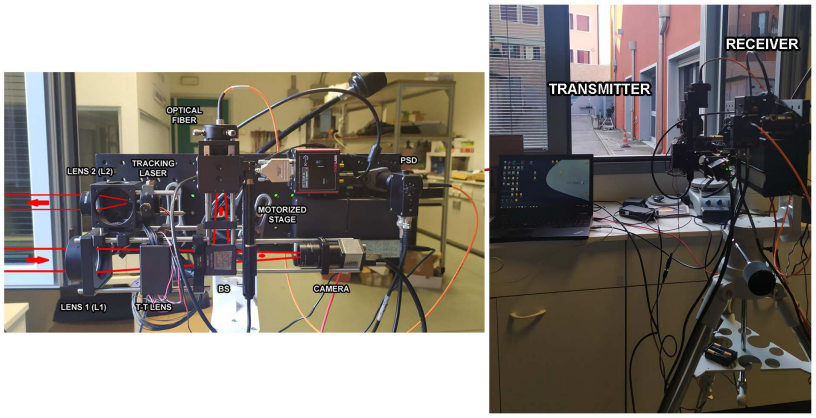

Figure 4.4: Receiver setup of the FSO comunication system.

As first we aligned the communication system with the transmission laser located in the transmitter, once we centered the beam we moved the receiver mount to center the tracking laser on the tracking camera placed in the transmitter. When the system has been fully aligned, we calibrated the tracking system and operated it to maintain alignment throughout the measurements. We performed the T-T lens calibration with *Photonloop* and closed the loop. At this point, the next step was to center the focused beam on the fiber. To get the spot into the fiber, we first tried to find the best z position and the x-y position manually. As voltage feedback we used a NI USB-6001 connected to the PSD detector. The manual procedure is not sufficient because moving the system manually slight misalignments occur. Furthermore an

higher precision is achieved with motorized positioning. To exactly match the entrance angle of the light into the fiber two more degrees of freedom should be controlled. In future developments of the system a secondary tip tilt lens could be introduced for this purpose. We developed a system that could find the best position in the x-y plane and the best focus position along the z direction (z_m) automatically. We then exploited the potential of the *T-T lens B*, with the use of the motorized stage, to create a fully automatic scan in the x-y-z directions: we performed a x-y scan with the T-T lens (from -0.03 to 0.03 waves in terms of tip and tilt modes) for several positions of the fiber along the z axis. The x-y scan has been performed measuring the voltage on the fiber with the ADC for each position on the scan windows (20x20) from z_m - 0.5 mm to z_m + 0.3 mm with a step of 0.2 mm. Since the turbulence could make the measurement less precise we decided to perform a stop of 0.5 seconds per position and considered the mean voltage measured by the ADC. The scan windows has been reduced by an increasing factor from 2 to 5 for each step along the z direction moving the center position of the scan to the previous maximum maintaining the same number of steps in order to improve the resolution. During the scan the tracking system was on and T-T lens operated in closed loop. The procedure scheme of the x-y scan for each z position is reported in Fig. 4.5. .

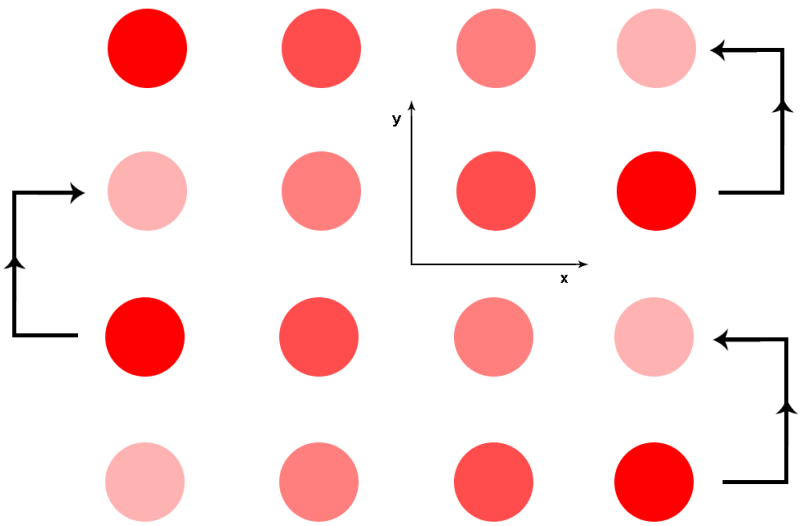

Figure 4.5: Scan procedure scheme on the x-y plane.

We have obtained a map of the measured voltage as function of the x-y position of the spot for each z position of the scan. The Fig. 4.6 shows 3 of the 5 scans performed during the fiber centering in the course of the experiment,

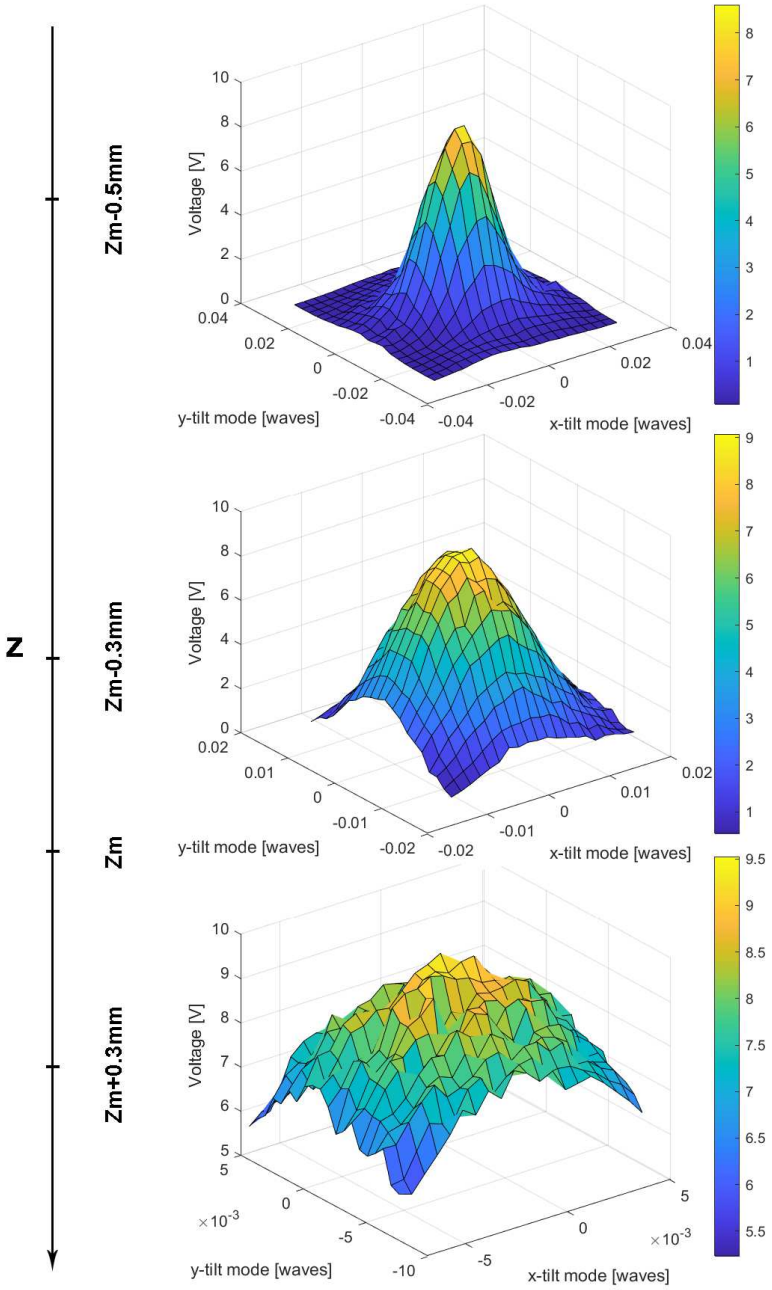

Figure 4.6: The x-y scan window is different for each step along the z position and centered on the maximum found in the previous scan. It is possible to see how the resolution and the detected voltage increase reaching a maximum value of 9.5 V while scanning along z.

in particular z= z_m - 0.5 mm, z= z_m - 0.3 mm and z=z_m + 0.3 mm. As we can see, scanning along z and reducing the scan window around the center we have been able to reach a fiber intensity of about 9.5 V against about 8.5 V of the first scan. At the end of the scan procedure we positioned the fiber at the right location in z with the motorized stage and set the spot to the right x-y position.
After the optimization of the injection of the laser into the fiber we performed the measurements of the Tip-Tilt lens performances with the *Photonloop* sotware and of the PSD voltage for the fiber coupling efficiency esteem with the NI USB 6001 in the following different cases:

- **A)** Fiber coupling efficiency analysis without *T-T lens B* correction and tracking.

- **B)** Fiber coupling efficiency analysis without *T-T lens B* correction keeping tracking active.

- **C)** Fiber coupling efficiency analysis performing *T-T lens B* closed loop correction keeping tracking inactive.

- **D)** Fiber coupling efficiency analysis performing *T-T lens B* closed loop correction keeping tracking active.

These measurements were made using a time interval of 3 minutes each. The error on the measured voltage $\sigma = 0.09\ V$ has been obtained from the standard deviation of a 3 minutes test with the FSO transmission system placed inside the laboratory in order to be free of aberrations. The *photonloop* settings used during all three cases are reported in Tab. 4.1:

Photonloop settings	
Framerate [Hz]	≈ 1000
Focal length [mm]	300
Pizel size [mm]	$5.8 \cdot 10^{-3}$
Wavelength [μm]	0.808

Table 4.1

4.3 Results

The fiber voltage analysis results for the cases A, B, C and D are reported below in Fig. 4.7 and in Tab. 4.2:

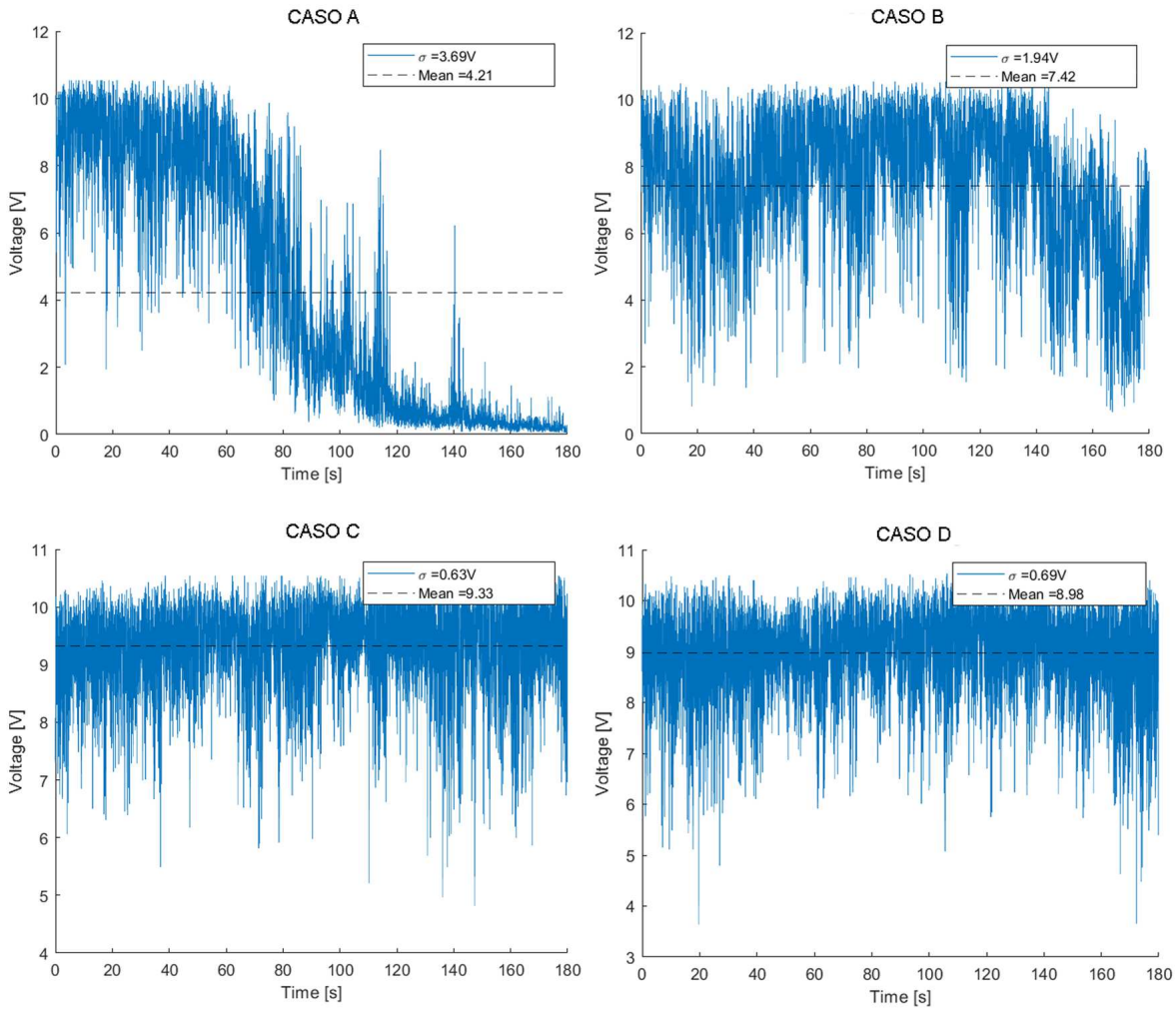

Figure 4.7: PSD voltage results where the blue line indicates the measured intensity value over the time.

.

	Case A Lens OFF Tracking OFF	Case B Lens OFF Tracking ON	Case C Lens ON Tracking OFF	Case D Lens ON Tracking ON
Standard dev. (σ)	3.69 V	1.94 V	0.63 V	0.69 V
Mean Voltage	4.21 V	7.42 V	9.33 V	8.98 V

Table 4.2

To better understand these results, it is useful to compare the cases in order to highlight the advantages due to the presence of the tracking system and the correction performed by the lens.

4.3.1 First Comparison (Case A - Case B)

In this first comparison we wanted to evaluate the presence of the tracking system without the T-T lens correction. The difference between the case A (uncorrected case) and the case B (corrected case) has been reported in the next graphs . .

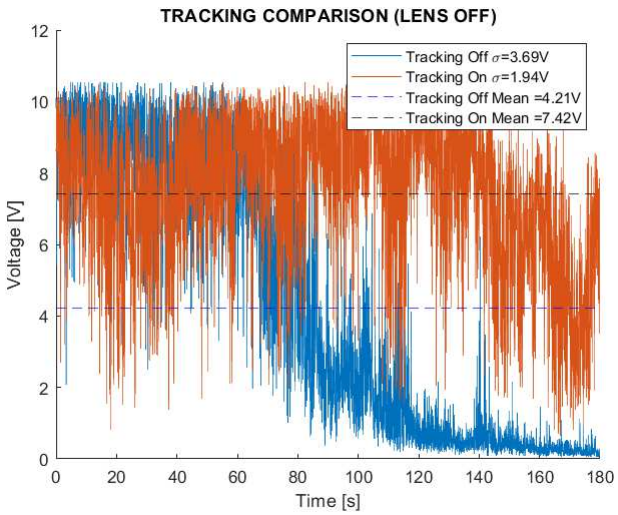

Figure 4.8: Fiber voltage distribution over time in the first comparison between case D and case B. *Orange line*: Case B ; *blue line*: Case A.

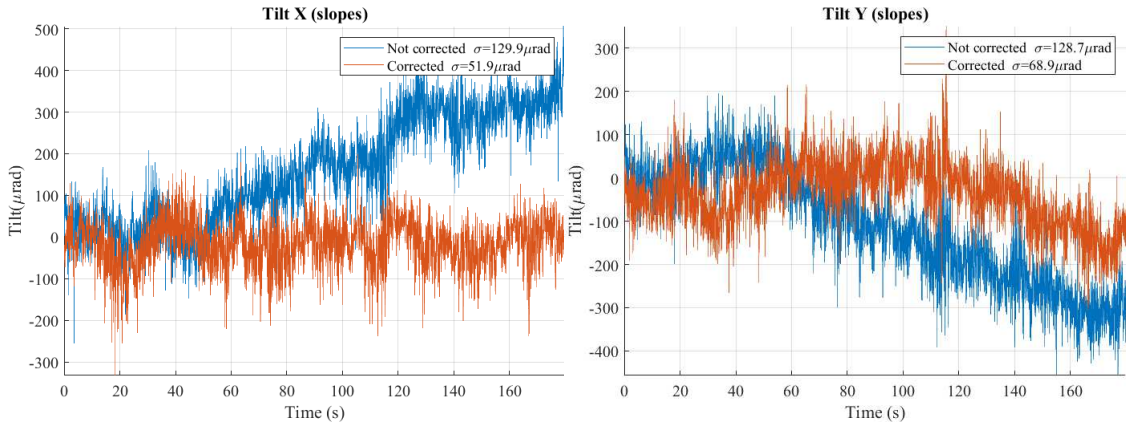

Figure 4.9: Tilt X and Tilt Y values (μrad); *orange line*: tilt value in case B ; *blue line*: tilt value in case A.

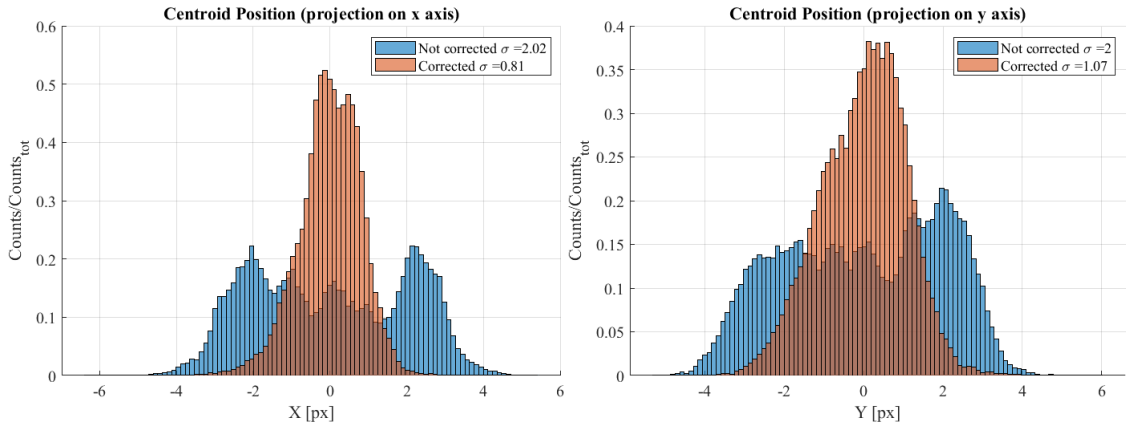

Figure 4.10: This figure reports the distribution of the centroids projected on the two axis X and Y; *orange*: case B ; *blue*: case A.

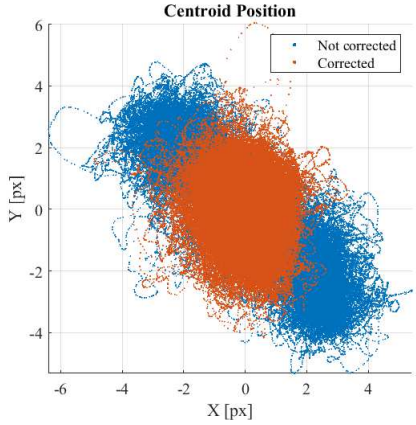

Figure 4.11: The distribution on the X-Y plane of the centroids is reported; *orange*: case B ; *blue*: case A.

from the Fig. 4.8 we can see that the tracking system leads encouraging results, improving the standard deviation of the uncorrected case $\sigma = 3.69$ V to $\sigma = 1.94$ V for the corrected case. These measure is affected by a progressive drift of the spot on the detector due to the absence of the mounts tracking. In this way the system has not been able to compensate for misalignments introduced by the wind or by an imperfect fixing of the mounts. It can be seen also in Fig. 4.9 where the blue lines shows the effect of the drift in both tilt directions and in Fig. 4.10 where the centroid positions projected on x and y axis are reported. The effectiveness of the tracking system is clear, in the corrected case the beam did not suffer from drifting or displacement but only from the atmospheric turbulence. The turbulence in this comparison has not been corrected because our attention was turned to the advantages of the tracking system keeping the lens correction inactive.

4.3.2 Second Comparison (Case B - Case D)

The second comparison is characterized the presence of the T-T lens correction and tracking system with respect to the only presence of the mounts tracking. The difference between the case B (uncorrected case) and the case D (corrected case) has been reported in the next figures.

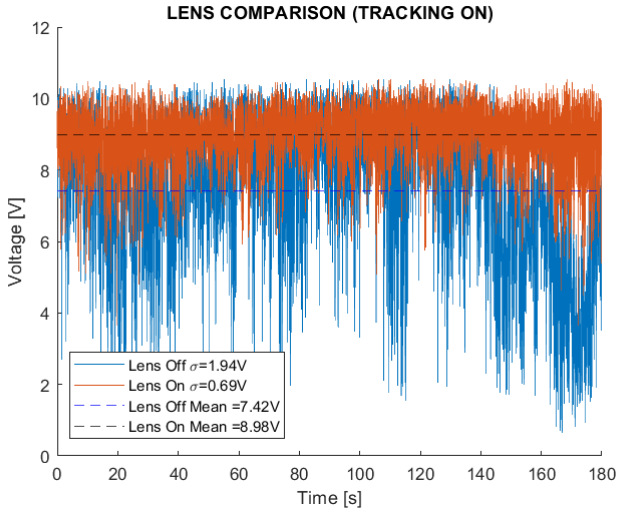

Figure 4.12: Fiber voltage distribution over time in the first comparison between case B and case D. *Orange line*: Case D ; *blue line*: Case B.

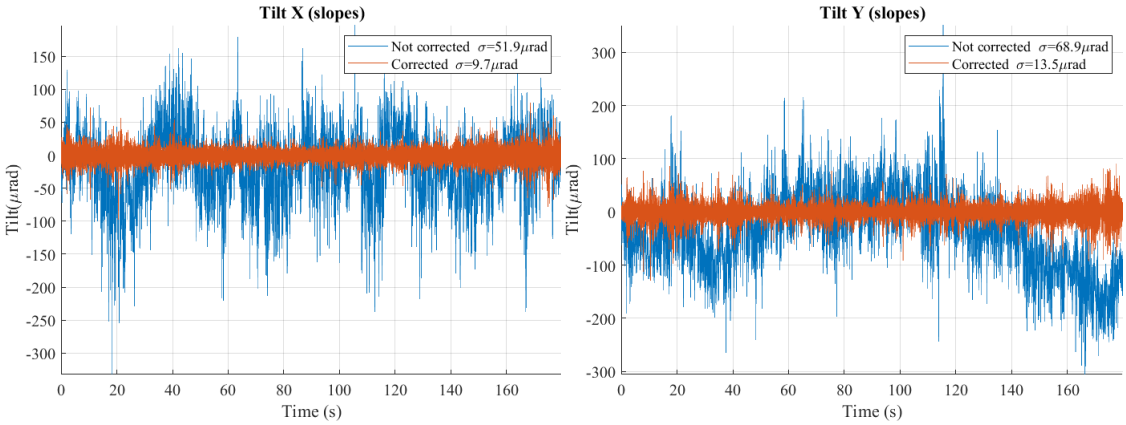

Figure 4.13: Tilt X and Tilt Y values (μrad); *orange line*: tilt value in case D ; *blue line*: tilt value in case B.

.

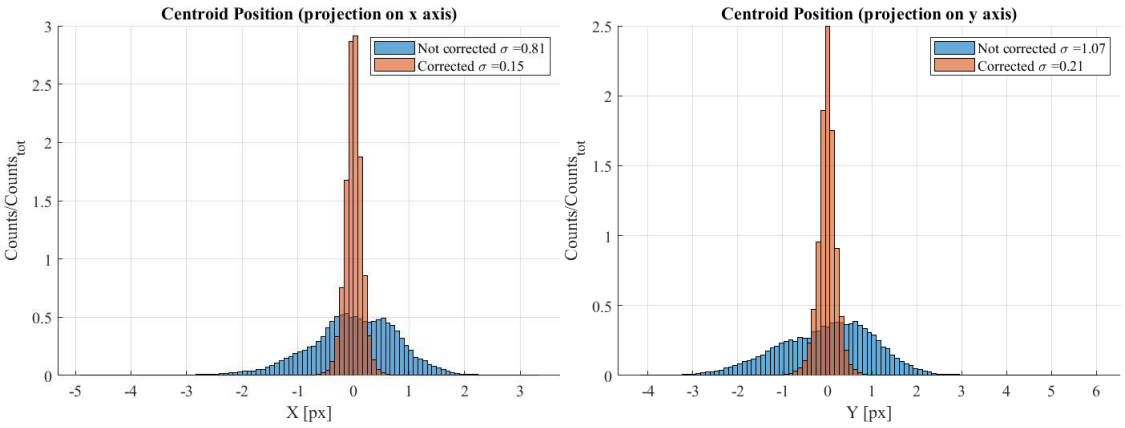

Figure 4.14: This figure reports the distribution of the centroids projected on the two axis X and Y; *orange*: case D ; *blue*: case B.

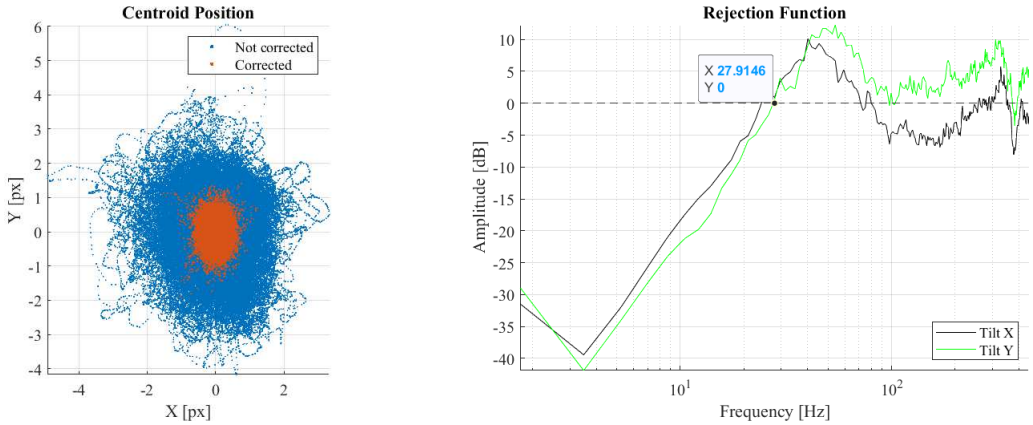

Figure 4.15: on the left panel the distribution on the X-Y plane of the centroids is reported; *orange*: case D ; *blue*: case B. On the right side is shown the rejection function; *black*: Tilt X ; *green*: Tilt Y.

from the Fig. 4.12 we can see that the lens has been able to correct the aberrations , improving the standard deviation from $\sigma = 1.94$ V for the uncorrected case (with tracking) to $\sigma = 0.69$ V for the corrected case, about 64% less. With the closed loop correction of the lens we have been able to reach a mean value of 8.98 V instead of 7.42 V of the uncorrected case, near 21% of increasing. From the Fig. 4.14 and Fig. 4.15 we can retrieve the performances of the *T-T lens B*. The distribution of the centroids along the two axis is significantly more compact, 73% for the y axis and 82% for the x axis with respect to the standard deviation of the uncorrected case. The

rejection band obtained gave us a cutoff frequency near 28 Hz for tilt y and 24 Hz for tilt x.

4.3.3 Third Comparison (Case C - Case D)

The third and last comparison is between the case with the T-T lens correction and tracking system active and the case with the only presence of the lens. The difference between the case C (uncorrected case) and the case D (corrected case) has been reported below.

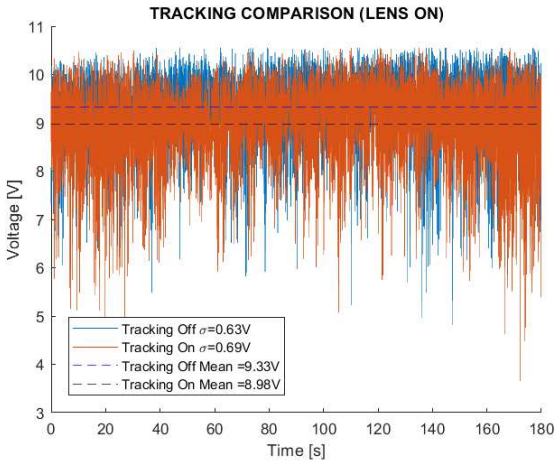

Figure 4.16: Fiber voltage distribution over time in the first comparison between case C and case D. *Orange line*: Case D ; *blue line*: Case C.

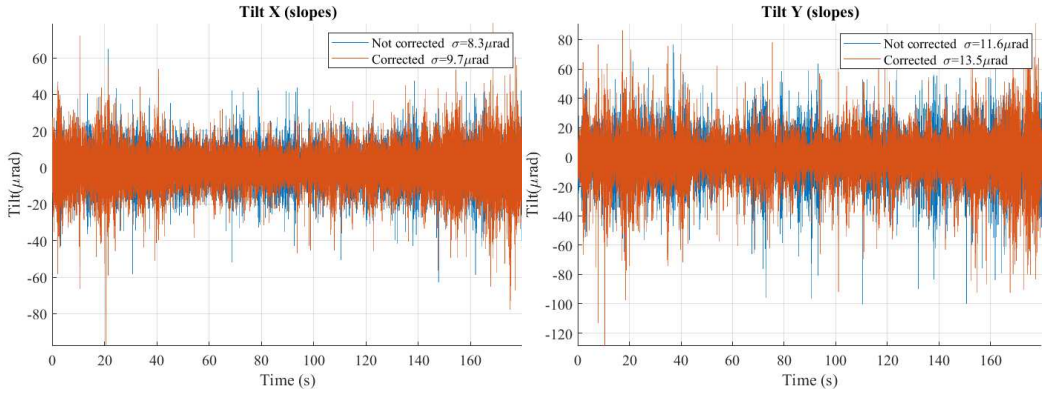

Figure 4.17: Tilt X and Tilt Y values (μrad); *orange line*: tilt value in case D ; *blue line*: tilt value in case C.

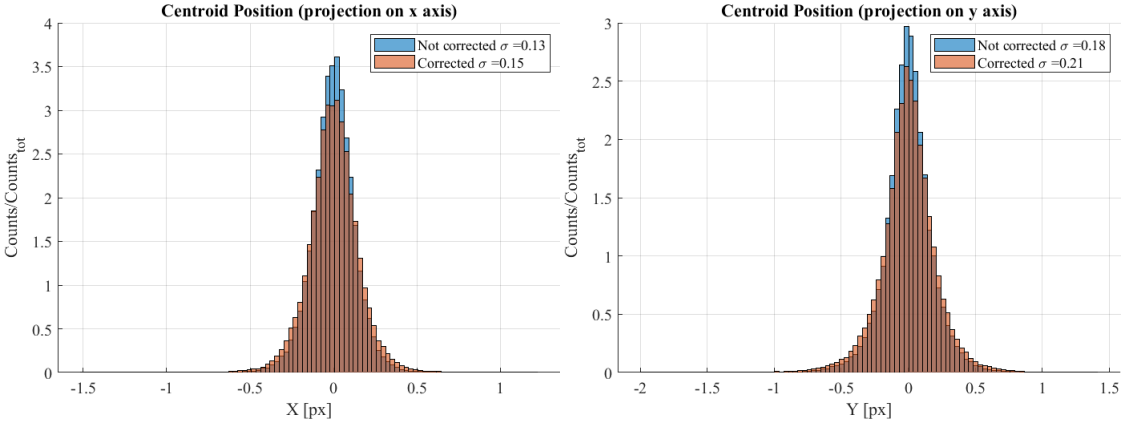

Figure 4.18: This figure reports the distribution of the centroids projected on the two axis X and Y; *orange*: case D ; *blue*: case C.

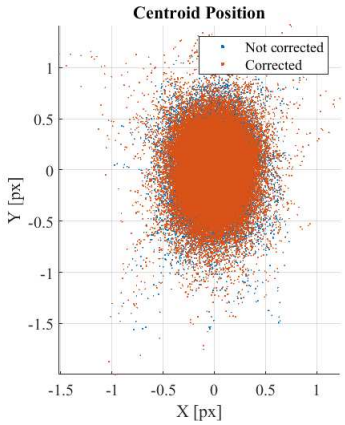

Figure 4.19: on the left panel the distribution on the X-Y plane of the centroids is reported; *orange*: case D ; *blue*: case C.

From the results of this comparison we can see that in the short period (3 minutes) and in a situation of short distance between transmitter and receiver the lens correction is able to maintain the beam centered on the detector without the help of the tracking system; indeed the tracking does not improve the fiber coupling giving the similar results we obtained in this two cases.
This preliminary tests give very encouraging results about the potential improvements that the T-T lens can bring to the laser transmission. However, the measurements have been carried for 3 minutes, quite a small time compared to the working time of a real FSO telecommunications system. For this reason we observed the behavior of the beam during one hour with the

mounts tracking system and the closed-loop correction by the lens both active. The result is reported in Fig. 4.20. As we can see the system has been able to maintain the same degree of correction for the entire period of time, obtaining a standard deviation of $2\sigma = 1.51$ V and an average intensity value into the fiber of 9.27 V.

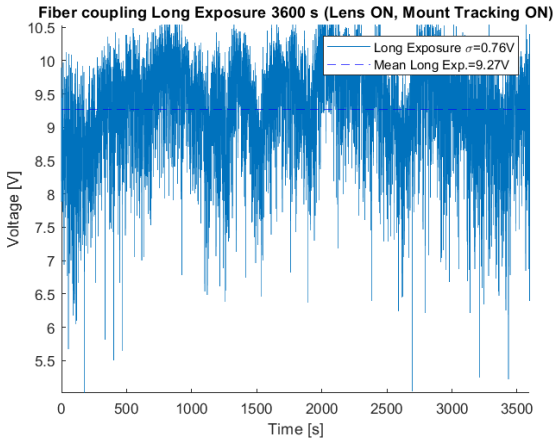

Figure 4.20: Fiber voltage distribution in a time interval of 3600 s.

Conclusions

In this thesis work, we studied an adaptive optics system for the improvement of the performances of short free space communication links to be used in urban environments. The main component of the system is a a refractive deformable element that is easy to integrate into compact telecommunications systems capable of decreasing the bit error rate caused by atmospheric turbulence by increasing fiber coupling efficiency. During my time in the CNR-IFN Laboratories in Padova, we developed two generations of tunable lenses, able to correct Tip and Tilt aberration. The two lenses presented 2 and 4 actuators respectively with maximum actuators strokes of $\pm 63 \mu m$ and $\pm 106 \mu m$ for the lens A and $\pm 41 \mu m, \pm 44 \mu m, \pm 40 \mu m, \pm 39 \mu m$ for the lens B. The two lenses are different also in terms of performances. With respect to the lens A (first generation) the second release, lens B, was designed to have higher resonant frequencies ($\geq$ 900 Hz) and therefore higher stability. We tested the T-T lens B in the laboratory with an experiment that simulates a real outdoor horizontal transmission where the source of aberration was performed by a multi actuator deformable lens. This analysis has brought good results highlighting an improvement of about 60% of the rejection of the Tilt along the two axis. The T-T lens B has been later tested with a 20 m FSO horizontal transmission of a collimated laser between two telescope mounts. The beam has been focused and injected into a multi-mode optical fiber with the Tip and Tilt correction performed by the T-T lens B in closed loop. For this outdoor experiment we also developed an active tracking system for long term and large amplitude drifts. Using our mounts tracking system we have been able to achieve an increase in fiber intensity of about 21% more than what we measured without T-T lens correction. We reached, also, a reduction in the variance of the fiber coupling of about 64%. Through the analysis on the distribution of centroids as a function of time we obtained an improvement on the dispersion of about 73% along the y axis and 82% along the x axis. The first comparison shown the effectiveness of the tracking system highlighting a progressive drift of the spot on the detector in absence of the mounts tracking. Many improvements can be made

to the system in the future to make it even more accurate and performing; for example it could be introduced a second T-T lens in order to adjust the fiber entry angle, the composition of the lens can certainly be improved by replacing the slides with better performing surfaces and, in addition to these, an upgrading of the actuators can be evaluated to make the lens more stable and precise. This experiment has been the basis for the development of a new type of compact free space communication module that will be tested in the next months in CNR laboratories.

Appendix A

Tip-Tilt lens A

A.1 Piezoelectric actuators hysteresis

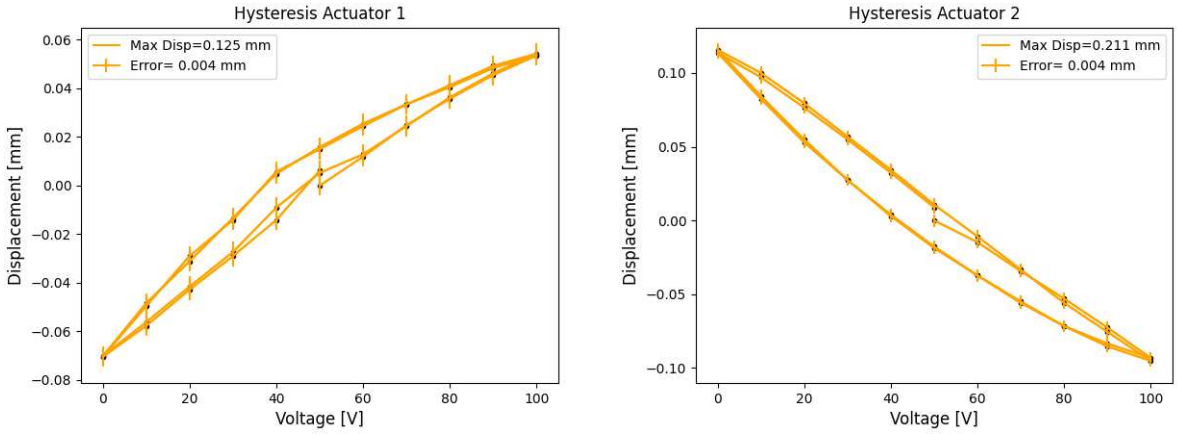

Figure A.1: Hysteresis cycles of the two piezoelectric actuators used in *T-T lens A*

A.2 Design

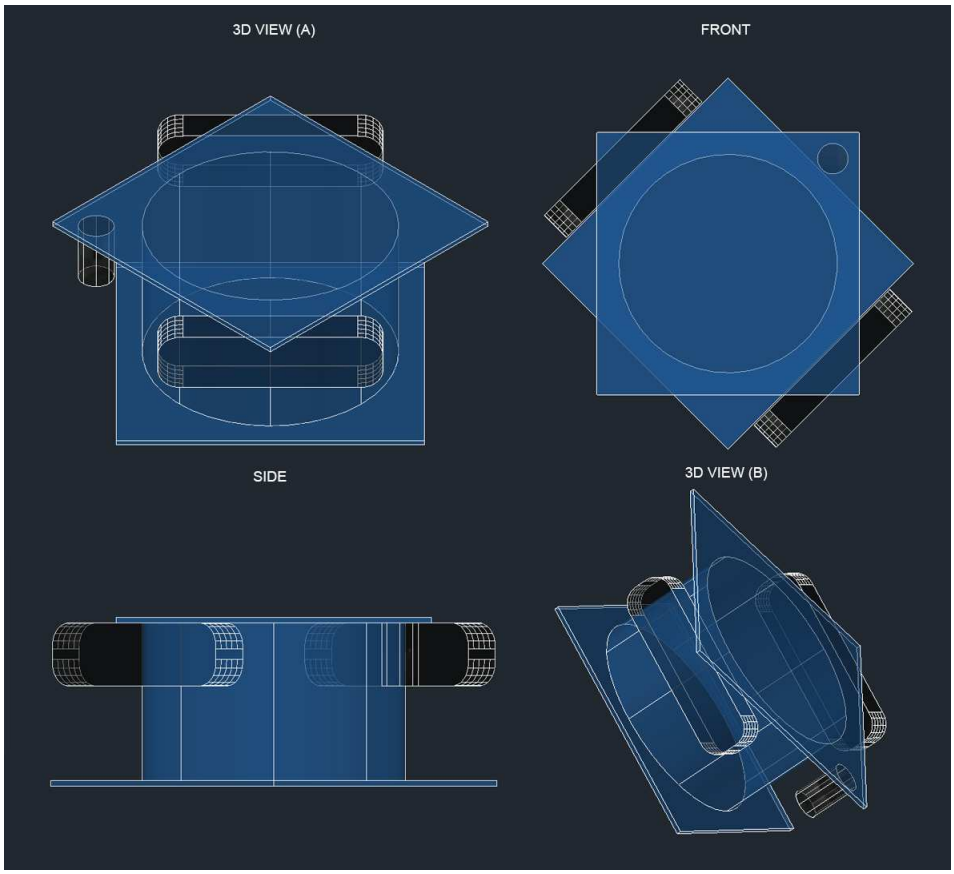

Figure A.2: Sketch of the *T-T lens A design.*

Bibliography

[1] A. Alkholidi and K. Altowij, *Effect of Clear Atmospheric Turbulence on Quality of Free Space Optical Communications in Western Asia*, 03 2012.

[2] H. W. Babcock, *The Possibility of Compensating Astronomical Seeing*, , 65 (1953), p. 229.

[3] S. Bonora, Y. Jian, P. Zhang, A. Zam, E. N. Pugh, R. J. Zawadzki, and M. V. Sarunic, *Wavefront correction and high-resolution in vivo oct imaging with an objective integrated multi-actuator adaptive lens*, Opt. Express, 23 (2015), pp. 21931–21941.

[4] D. Casasent, *Performance evaluation of spatial light modulators*, Applied Optics vol. 18 iss. 14, 18 (1979).

[5] J. R. Crepp, *Improving planet-finding spectrometers*, Science, 346 (2014), pp. 809–810.

[6] D. Damjanovic, *Hysteresis in Piezoelectric and Ferroelectric Materials*, vol. 3, 01 2006, pp. 337–465.

[7] J. DEMPSTER, *Chapter six - signal analysis and measurement*, in The Laboratory Computer, J. DEMPSTER, ed., Biological Techniques Series, Academic Press, London, 2001, pp. 136–171.

[8] N. K. Dhar, R. Dat, and A. K. Sood, *Advances in infrared detector array technology*, in Optoelectronics, S. L. Pyshkin and J. M. Ballato, eds., IntechOpen, Rijeka, 2013, ch. 7.

[9] S. DiFilippo, *Optical design of Wavefront Sensor for Laser Guide Stars for Ground Based Telescopes*, 2018.

[10] DOW, *Dowsil™ q3-6575 dielectric gel.* https://www.dow.com/content/dam/dcc/documents/en-us/productdatasheet/11/11-12/11-1279-dowsil-q3-6575-dielectric-gel.pdf?iframe=true.

[11] D. F. Edwards, *Adaptive Optics Engineering Handbook, by Robert K. Tyson*, Optics & Photonics News, 11 (2000), p. 46.

[12] N. N. C. for Environmental Information, *U.s. wind climatology.* https://www.ncdc.noaa.gov/societal-impacts/wind/.

[13] M. C. Gokce, Y. Baykal, and Y. Ata, *Adaptive optics effect on performance of bpsk-sim oceanic optical wireless communication systems with aperture averaging in weak turbulence*, Journal of Quantitative Spectroscopy and Radiative Transfer, 256 (2020), p. 107335.

[14] Z. Hai, S. Lu, Q. Zhai, B. Huang, Y. Long, Y. Zhao, and D. Li, *Simulation and experiment of a diamond-type micro-displacement amplifier driven by piezoelectric actuator*, The Journal of Engineering, 2020 (2019).

[15] S.-B. C. Y.-M. Han, *Piezoelectric actuators : control applications of smart materials*, CRC Press, 2010.

[16] N. Instrument, *Pid theory explained - ni.* https://www.ni.com/it-it/innovations/white-papers/06/pid-theory-explained.html.

[17] P. Instrumente, *Picma stack multilayer piezo acutators.* https://www.physikinstrumente.com/en/?type=5600downloadUid=838downloadFileUid=746.

[18] A. Jahid, M. H. Alsharif, and T. J. Hall, *A contemporary survey on free space optical communication: Potential, technical challenges, recent advances and research direction*, CoRR, abs/2012.00155 (2020).

[19] H. Li, Y. Xu, M. Shao, L. Guo, and D. An, *Analysis for hysteresis of piezoelectric actuator based on microscopic mechanism*, 399 (2018), p. 012031.

[20] J. Liu, V. Muruganandan, R. Clare, M. C. Ramirez Trujillo, and S. Weddell, *A tip-tilt mirror control system for partial image correction at uc mount john observatory*, 11 2020, pp. 1–6.

[21] N. Md and M. Bhuiyan, *Effect of operating wavelengths and different weather conditions on performance of point-to-point free space optical link*, International journal of Computer Networks Communications, 8 (2016), pp. 63–75.

[22] F. Merkle, P. Kern, P. Léna, F. Rigaut, J. C. Fontanella, G. Rousset, C. Boyer, J. P. Gaffard, and P. Jagourel, *Successful tests of adaptive optics.*, The Messenger, 58 (1989), pp. 1–4.

[23] N. Mohammed, A. El-Wakeel, and M. Aly, *Pointing error in fso link under different weather conditions*, International Journal of Video Image Processing and Network Security IJVIPNS-IJENS, 12 (2012), p. 6.

[24] A. Montmerle Bonnefois, J. M. Conan, C. Petit, C. B. Lim, V. Michau, S. Meimon, P. Perrault, F. Mendez, B. Fleury, J. Montri, and N. Védrenne, *Adaptive optics pre-compensation for GEO feeder links: the FEEDELIO experiment*, in International Conference on Space Optics — ICSO 2018, vol. 11180 of Society of Photo-Optical Instrumentation Engineers (SPIE) Conference Series, July 2019, p. 111802C.

[25] R. J. Noll, *Zernike polynomials and atmospheric turbulence.*, Journal of the Optical Society of America (1917-1983), 66 (1976), pp. 207–211.

[26] S. S. Olivier and D. T. Gavel, *Tip-tilt compensation for astronomical imaging.*, Journal of the Optical Society of America A, 11 (1994), pp. 368–378.

[27] J. Pilar, *Adaptive Optics for high average-power laser systems*, 2016.

[28] R. Ragazzoni, *Pupil plane wavefront sensing with an oscillating prism*, Journal of Modern Optics, 43 (1996), pp. 289–293.

[29] L. Roberts, G. Block, S. Fregoso, H. Herzog, S. Meeker, J. Roberts, J. Tesch, T. Truong, J. Rodriguez, and A. Bechter, *First Results from the Adaptive Optics System for LCRD's Optical Ground Station One*, in The Advanced Maui Optical and Space Surveillance Technologies Conference, S. Ryan, ed., Sept. 2018, p. 3.

[30] F. Roddier, *Adaptive Optics in Astronomy*, 2004.

[31] M. C. Roggemann and B. Welsh, *Imaging through turbulence*, 1995.

[32] J. Sakamoto and H. Barrett, *Inverse optical design and its applications*, Optics InfoBase Conference Papers, (2011).

[33] A. Sharma and R. S. Kaler, *Designing of high-speed inter-building connectivity by free space optical link with radio frequency backup*, Communications, IET, 6 (2012), pp. 2568–2574.

[34] O. M. Solomon, Jr, *Psd computations using welch's method. [power spectral density (psd)]*.

[35] V. I. Tatarskii, *Wave Propagation in Turbulent Medium*, 1961.

[36] R. K. Tyson, *Principles of adaptive optics*, 1998.

[37] H. J. White, D. W. Gough, R. Merry, and S. Patrick, *Demonstration of free-space optical communication link incorporating a closed-loop tracking system for mobile platforms*, in Advanced Free-Space Optical Communications Techniques and Technologies, M. Ross and A. M. Scott, eds., vol. 5614 of Society of Photo-Optical Instrumentation Engineers (SPIE) Conference Series, Dec. 2004, pp. 119–128.

[38] YOUTREND.IT, *Italia digitale: l'evoluzione degli ultimi 10 anni*.

[39] G. Zhu, J. Lévine, L. Praly, and Y.-A. Peter, *Flatness-based control of electrostatically actuated mems with application to adaptive optics: A simulation study*, Journal of Microelectromechanical Systems, 15 (2006).

[40] A. Ziad, *Review of the outer scale of the atmospheric turbulence*, in Adaptive Optics Systems V, E. Marchetti, L. M. Close, and J.-P. Véran, eds., vol. 9909 of Society of Photo-Optical Instrumentation Engineers (SPIE) Conference Series, July 2016, p. 99091K.